Numerical modeling of liquid jets in crossflow with applications to supersonic combustion ramjets

by

Wyatt A. Hagen

A thesis submitted to the graduate faculty

in partial fulfillment of the requirements for the degree of

MASTER OF SCIENCE

Major: Aerospace Engineering

Program of Study Committee:
Alric Rothmayer, Major Professor
Jonathan Regele
Shankar Subramaniam

The student author, whose presentation of the scholarship herein was approved by the program of study committee, is solely responsible for the content of this thesis. The Graduate College will ensure this thesis is globally accessible and will not permit alterations after a degree is conferred.

Iowa State University

Ames, Iowa

2017

TABLE OF CONTENTS

LIST OF TABLES

LIST OF FIGURES

ACKNOWLEDGEMENTS

I would like to thank all of those who assisted me throughout this research. First, I would like to thank my program of study committee. Prof. Rothmayer for his willingness to take over the roll of Major Professor for my research and provide guidance throughout the writing of this thesis. Prof. Subramaniam for providing guidance and new ideas for the project. Lastly, Prof. Regele for his guidance and knowledge throughout the completion in this work. I am especially grateful for the opportunities he provided to explore this exciting topic and his challenge to me to continually test my limits.

I would also like to thank all the members of the Computational Multi-Phase and Combustion Research Laboratory during the duration of my research. I greatly appreciate all of the insight provided and research oriented discussion–particularly those held late into the night. Every member made an impact on my studies and for that I am grateful.

Lastly, I want to thank all my family and friends whose support throughout this work was immeasurable.

ABSTRACT

Liquid jets in crossflow are used in a variety of fuel injection systems. Of particular interest in this work is the injection of liquid fuel into supersonic crossflow at scramjet startup conditions. Due to the short residence times of fuel in the combustor, it is imperative to efficiently and rapidly atomize and mix the fuel. Experiments often have limited ability to observe all of the wide range of scales and complicated liquid structures present in these conditions. Numerical simulations can provide additional insights into these complex flows. In this work, a numerical approach for the solution of compressible multi-component flows with capillary effects is presented along with additions to enable the solution of large computational problems The approach is then validated against a non-turbulent round jet in subsonic crossflow. Comparisons to jet trajectory, column breakup location, and instability wavelengths are completed. A liquid jet in supersonic crossflow is simulated and the effects of a turbulence in the jet inflow are investigated. The jet trajectory is compared against experimental results. Although differences between the experimental results and numerical simulations are observed, the results suggest jet inflow turbulence can impact the atomization process in supersonic crossflow conditions and quantification of inflow conditions is important.

CHAPTER 1. INTRODUCTION AND LITERATURE REVIEW

Liquid jets in crossflow, or transverse jets, are frequency used in the atomization of fuels in a variety of fuel injection systems. Transverse jets play an important role in gas turbines, afterburners, and ramjet and scramjet combustors [47, 77]. The breakup process is a significant consideration as the efficiency of the combustions process relies heavily on the atomization of the fuel [28]. A number of experimental, analytical, and computational studies have investigated the characteristics of transverse liquid jets.

One particular current challenge is the atomization of liquid fuel during scramjet startup conditions. In scramjet combustors the efficiency depends strongly on the ability to efficiently and quickly atomize liquid fuel due to the short residence time of the fuel in the combustor [8, 11, 16]. Total residence times of air for a scramjet are on the order of a millisecond from the inlet to the engine nozzle [11]. Thus, the injected fuel must mix with the incoming air and burn within hundredths of a millisecond to achieve efficient combustion [11]. This highlights the importance of injected liquid atomizing efficiently and mixing with crossflow quickly in the scramjet combustor.

A number of experimental results for the atomization of liquid jet in supersonic crossflow exist [35, 41–43, 83]. These experimental results often quantify a number of large scale features including jet trajectory and penetration [41, 83], mean droplet properties [42], and droplet distribution profiles [43] through the use of various experimental techniques such as shadowgraphs [41] and Phase Doppler Particle Analysis (PDPA) [42].

However, due to the range of scales and complicated liquid features experiments are frequently limited in the ability to provide a complete physical picture [47]. Numerical simulations can provide additional insights in the understanding of these complex flows. Computational results can provide both a qualitative and quantitative picture of the flow field that is often difficult or infeasible to obtain in experimental tests. However, while a wide body of computational results exists in subsonic crossflow [26, 39, 57, 78], little work has been done on atomization in supersonic crossflows.

1.1 Atomization of Liquid Jets

The breakup of liquid jets is divided into two classifications, primary and secondary breakup [13, 76]. Primary breakup involves the breakup of liquid columns into ligaments and droplets, while secondary atomization consists of the breakup of the ligaments and droplets into smaller ligaments and droplets. An example of the breakup process is shown if Fig. 1.1.

A liquid jet is injected transversely at 90 degrees relative to the crossflow. Aerodynamic forces on the jet result in the column deformation flattening the cross-section. Instability waves develop on the surface of the liquid column which grow in strength. Eventually these waves lead to the breakup of the liquid column resulting in the creation of ligaments and droplets [77]. These ligaments and droplets then undergo secondary breakup as they travel downstream. In addition, droplets and ligaments can be stripped from the liquid column by the gas flow around the column depending on the velocity of the crossflow [47]. This process is often referred to as surface breakup [6] or shear breakup as aerodynamic forces strip off liquid through shear forces [45].

A similar process is present in supersonic crossflows [38]. Additional features include the appearance of a bow shock in front of the liquid column along with a separation region and separation shock [83].

Figure 1.1 Example of the breakup process for a liquid jet in crossflow.

1.2 Literature Review

Liquid jets in crossflow have been studied in a variety of experimental conditions. Hojnacki looked at liquid jets in crossflow at medium subsonic Mach numbers and their use in ramjet fuel injection at the Air Force Aero Propulsion Laboratory [28]. The goal of the work was to develop empirical methods to assist in the design of fuel system, a common theme throughout the literature. Penetration heights and column trajectories were investigated and correlations were developed. In addition, the effect of viscosity was found not to effect the penetration. Yates looked at jet in supersonic crossflow also at the Air Force Aero Propulsion Laboratory investigating the penetration height. A theoretical model to predict transverse distribution of the liquid mass was developed using the results [83]. Kush and Schetz also looked that the penetration of liquid jet in supersonic crossflows and their penetration [35]. Schetz et al. investigated transverse jets with crossflow Mach numbers at higher subsonic speeds of 0.45 and 0.75 investigating

the effect of injector geometry using round and rectangular injectors [66]. With this data penetration correlations were investigated along with droplet size distribution. Schetz et al. expanded on this work in [65] using supersonic crossflows from Mach 2.4-4.0. A variety of liquids where used and the development of large waves on liquid column were investigated. Nejad and Schetz reviewed the effects of viscosity on a jet in supersonic crossflow in addition to looking at the effects of surface tension [52]. They added ethyl alcohol to water to reduce the surface tension and glycerine to increase viscosity. A 22% difference in penetration was reported for the more viscous liquid jets than water as opposed to the subsonic work of Hojnacki [28] while the surface tension had little effect. Both surface tension and viscosity were found to have effects on surface wavelengths. Wu et al. studied a wide range of operating conditions for non-turbulent jets and developed a breakup process map [77]. In addition, correlations for column fracture location and jet trajectory were developed. The surface waves were investigated further in Mazallon et al. and a correlation of the wavelength to crossflow Weber number was developed [48]. Sallam et al. extended on the work of Wu and Mazallon using pulsed holography to further investigate the breakup regimes and surface wavelengths. They also looked at the column fracture location, liquid surface properties, and droplet properties. Lee expanded on the work of Sallam et al. to turbulence liquid jets in crossflow and comparing the effect on turbulence to the previous non-turbulent results [36]. Lin et al. investigated liquid jets in supersonic crossflows and investigated both pure and aerated-liquid jets [41, 42]. Shadowgraphs and phase doppler particle analyzer (PDPA) systems were used to measure liquid penetration. An investigation into hypersonic crossflow was carried out in Perurena et al. investigating penetration height, lateral extension, and mixing [59]. They also looked at the frequency of clump detachment and the fluctuations of the bow shock. Osta and Sallam investigated the effects of nozzle geometry on the liquid jet in turbulent liquid conditions and determined that L/D of the injector nozzle plays a role in the breakup length as well as breakup characteristics of the jet [55]. Lin et al. also looked

at two different nozzle geometries in the effect of supersonic crossflow and observed differences in penetration for aerated liquid jets [43].

Due to difficulty in resolving the near-field region in experiments numerical simulations can prove to be extremely insightful, for example direct numerical simulations [6]. This can become even more critical in the high crossflow Weber number flows often encountered in supersonic crossflows due to the increased crossflow velocities. Early work in to computational simulations often used two dimensional simulations. Heister et al. used two dimensional simulations of the Euler equations for a gas around a slice of the liquid column [25]. Using a force balance in the two dimensional slice along with mass and momentum conservation they could predict the trajectory of the liquid jet. Aalburg et al. also used two dimensional slices to simulate the liquid jet using the Navier-Stokes equations [1]. They assumed the vertical liquid jet velocity remains constant the deflection of the jet is modest. Their results showed good agreement with the vortex shedding frequency of the column and jet deflection.

Only more recently has the ability to perform detailed numerical simulations of liquid jets in crossflow in three dimensions become computationally feasible, however they are still quite computationally costly [47]. In subsonic flow a number of detailed computational simulations have been performed. Pai et al. performed and investigation of the primary breakup of a liquid jet in crossflow [57]. They found a good match with experimental correlations. The simulations suggested however that liquid Weber number may drive the surface waves as opposed to crossflow weber number. Hermann simulated the primary atomization of a turbulent liquid jet with varying density ratios and found density ratio has an effect on primary atomization [27]. Xiao et al. along with Owkes and Desjardins compared the effect of turbulence in the liquid jet inlet in subsonic conditions [56, 78]. Their results showed differences in trajectory and breakup between the laminar and turbulent cases simulated. In addition Xiao showed good agreement with the non-turbulent round jet results of Sallam et al. [63].

In the supersonic regime there is limited computational work without the use of atomization models either analytical, empirical, or subgrid models [25, 29–31, 44]. One exception is the work of Xiao et al. where primary breakup in a supersonic crossflow was simulated [80]. The approach coupled a compressible solver for the gas and an incompressible solver for the liquid. Another exception is the work of Garrick et al. who developed a fully compressible method for modeling atomization in compressible flows and demonstrated the ability to investigate the atomization of a liquid jet [19].

1.3 Objective

The objective of this work is to first validate the method developed in Garrick et al. [19] against experimental results for a liquid jet in subsonic crossflow. A jet in supersonic crossflow will then be simulated and liquid trajectory compared to supersonic empirical correlations. The effect of turbulence on the liquid jet will be investigated and a qualitative discussion of the observed near field region will be presented.

1.4 Thesis Outline

The remainder of the thesis is arranged in the following manner. The numerical approach is presented in chapter 2. In this section the governing equations are presented and are followed by the numerical method.

Additions to the solver to enable the solution of large computational problems through the use of rectilinear grids and distributed parallelization are discussed in chapter 3. The scaling efficiency of the resulting approach is investigated. Next, the generation of turbulent fluctuations and the implementation of a turbulent inflow is presented.

The simulation of a liquid jet in subsonic crossflow completed in chapter 4. The computational setup is discussed followed by a qualitative discussion of the simulation.

The results of the simulation are then analyzed and compared to experimental data to validate the numerical approach.

A supersonic crossflow is explored in chapter 5. After presenting the simulation conditions the results from non-turbulent and turbulent inflow cases are presented. The results are compared to experimental correlations for liquid jets in supersonic crossflow trajectory. In addition, the column fracture location is analyzed and compared to subsonic trends.

The results are summarized in chapter 6. Conclusions from the work are discussed. Finally, suggestions and directions for future work are presented for further investigation.

CHAPTER 2. NUMERICAL APPROACH

This chapter discusses the numerical approach of work. The numerical approach presented is based on the work of Garrick et al. [18–20]. The governing equations are presented and details of the numerical method and implementation are then discussed.

2.1 Governing Equations

The compressible multicomponent Navier-Stokes equations with capillary force terms govern the fluid flow for the problems to be considered [58]. In order to model the two-fluid problem the five equation model of Allaire is employed [2] utilizing a interface capturing approach [5, 68, 69]:

$$\frac{\partial \rho_1 \phi_1}{\partial t} + \nabla \cdot (\rho_1 \phi_1 \vec{V}) = 0 \tag{2.1}$$

$$\frac{\partial \rho_2 \phi_2}{\partial t} + \nabla \cdot (\rho_2 \phi_2 \vec{V}) = 0 \tag{2.2}$$

$$\frac{\partial \rho \vec{V}}{\partial t} + \nabla \cdot (\rho \vec{V}\vec{V} + p\bar{\bar{I}}) = \frac{1}{\mathrm{Re_a}} \nabla \cdot \bar{\bar{\tau}} + \frac{1}{\mathrm{We_a}} \kappa \nabla \phi_1 \tag{2.3}$$

$$\frac{\partial E}{\partial t} + \nabla \cdot ((E+p)\vec{V}) = \frac{1}{\mathrm{Re_a}} \nabla \cdot (\bar{\bar{\tau}} \cdot \vec{V}) + \frac{1}{\mathrm{We_a}} \kappa \nabla \phi_1 \cdot \vec{V} \tag{2.4}$$

$$\frac{\partial \phi_1}{\partial t} + \vec{V} \cdot \nabla \phi_1 = 0 \tag{2.5}$$

Equations 2.1 and 2.2 are continuity equations for the liquid and gas densities which are given by $\rho_1\phi_1$ and $\rho_2\phi_2$. The combined fluid density is given by ρ and individual fluid volume fractions by ϕ_1 and ϕ_2 for the liquid and gas respectively. Momentum conservation is provided by the vector set of Eqs. 2.3, where the vector velocity is given by $\vec{V} = \{u, v, w\}^T$, and total energy conservation by Eq. 2.4. The non-dimensional parameters $\mathrm{Re_a}$ and $\mathrm{We_a}$ are the acoustic Reynolds and Weber numbers, p is the pressure, and κ the interface curvature. The total energy, E, is given by

$$E = \rho e + \frac{1}{2}\rho\vec{V}\cdot\vec{V}, \tag{2.6}$$

where e is the specific internal energy. The viscous stress tensor is given by

$$\overline{\overline{\tau}} = 2\mu\left(\overline{\overline{D}} - \frac{1}{3}(\nabla\cdot\vec{V})\overline{\overline{I}}\right), \tag{2.7}$$

where

$$\overline{\overline{D}} = \frac{1}{2}\left(\nabla\vec{V} + (\nabla\vec{V})^T\right) \tag{2.8}$$

is the deformation rate tensor and μ is the non-dimensional mixture viscosity. A summary of the non-dimensionalizations used is presented in Table 2.1 where the 'stared'(*) quantities are the dimensional values and the reference state denoted by a '0' subscript.

Equation 2.5 is a transport equation for the volume fraction and is used in determining the interface location [2, 5]. The individual mass continuity equations discretely conserve the mass of both individual phases, and thus total mass as well. Surface tension is

Table 2.1 Non-dimensionalization used in the model

Parameter	**Rule**
Density	$\rho = \rho^*/\rho_0^*$
Velocity	$u = u^*/a_0^*$
Pressure	$p = p^*/\rho_0^* a_0^*$
Position	$x = x^*/l_0^*$
Time	$t = t^* a_0^*/l_0^*$
Acoustic Reynolds Number	$\mathrm{Re}_a = 1/\mu = \rho_0^*\, a_0^*\, l_0^*/\mu_0^*$
Acoustic Weber Number	$\mathrm{We}_a = 1/\sigma = \rho_0^*\, a_0^{*2}\, l_0^*/\sigma_0^*$

implemented through the use of the Continuum Surface Force model [58] with source terms in both the momentum and energy equations.

The diffuse interface capturing approach smears the material interface over multiple grid points. To model the fluid in this region it is treated as a mixture of the two fluids and mixture relations are needed to specify the properties [2, 9]. The mixture volume fraction of combination sums to unity:

$$\phi_2 = 1 - \phi_1. \tag{2.9}$$

Furthermore, the total density and internal energy are given by

$$\rho = \rho_1\phi_1 + \rho_2\phi_2 \tag{2.10}$$

and

$$\rho e = \rho_1\phi_1 e_1 + \rho_2\phi_2 e_2. \tag{2.11}$$

Assuming isobaric conditions at the interface the stiffened gas equation of state [24] is used to close the model

$$p = (\gamma - 1)\rho e - \gamma\pi_\infty. \tag{2.12}$$

Using this equation of state, the total energy can be rewritten as

$$E = \Gamma p + \Pi + \frac{1}{2}\rho\vec{V}\cdot\vec{V} \tag{2.13}$$

where Γ and Π are given by

$$\Gamma = \frac{1}{\gamma - 1} = \frac{\phi_1}{\gamma_1 - 1} + \frac{\phi_2}{\gamma_2 - 1}, \tag{2.14}$$

$$\Pi = \frac{\gamma\pi_\infty}{\gamma - 1} = \frac{\phi_1\gamma_1\pi_{\infty,1}}{\gamma_1 - 1} + \frac{\phi_2\gamma_2\pi_{\infty,2}}{\gamma_2 - 1}. \tag{2.15}$$

The properties of each fluid are dictated by the values for $\gamma_{1,2}$ and $\pi_{\infty,1,2}$. For gaseous fluids γ is taken to be equal to the physical value of gamma and $\pi_\infty = 0$. However,

for liquids both γ and π_∞ are fitting parameters used to match the behavior of the fluid [9, 50].

The speed of sound of the resulting mixture is given by

$$c = \sqrt{\frac{\gamma(p + \pi_\infty)}{\rho}} \tag{2.16}$$

with γ and π_∞ taken as the mixture values as given in Eqs. 2.14 and 2.15. Negative pressures can arise using the stiffened gas equation of state when modeling liquid phases [7, 14, 64, 67]. To ensure stability in the presence of negative pressures, $\gamma(p+\pi_\infty)$ is bounded to a small positive value when calculating the speed of sound [19]

$$\gamma(p + \pi_\infty) = \max(\gamma(p + \pi_\infty), 1.0 \times 10^{-9}). \tag{2.17}$$

Lastly, the mixture viscosity is given by [9, 58]

$$\mu = N\phi_1 + \phi_2 \tag{2.18}$$

where the liquid to gas viscosity ratio is defined as $N = \mu_1/\mu_2$.

In addition to the acoustic Reynolds and Weber numbers presented in Table 2.1, the crossflow Reynolds and Weber numbers are relevant to the description of a liquid jet in crossflow. These non-dimensional parameters are based on the crossflow freestream velocity u_0^*. These parameters are related to the respective acoustic parameters,

$$\mathrm{Re}_{\mathrm{cf}} = \frac{\rho_0^* u_0^* l_0^*}{\mu_0^*} = \mathrm{Re}_a \frac{u_0^*}{a_0^*} \tag{2.19}$$

$$\mathrm{We}_{\mathrm{cf}} = \frac{\rho_0^* u_0^{*2} l_0^*}{\sigma_0^*} = \mathrm{We}_a \frac{u_0^{*2}}{a_0^{*2}}, \tag{2.20}$$

and will be used in the simulation and analysis of atomization problems.

2.2 Numerical Method

The governing equations are discretized on a rectilinear grid in a finite volume approach.

$$\begin{aligned}\frac{\partial \vec{Q}_{i,j,k}}{\partial t} = &- \frac{1}{\Delta x}\left((\vec{f}_{i+1/2,j,k} - \vec{f}_{i-1/2,j,k})\right) \\ &- \frac{1}{\Delta y}\left((\vec{g}_{i,j+1/2,k} - \vec{g}_{i,j-1/2,k})\right) \\ &- \frac{1}{\Delta z}\left((\vec{h}_{i,j,k+1/2} - \vec{h}_{i,j,k-1/2})\right) + \vec{S}_{i,j,k}\end{aligned} \tag{2.21}$$

In this semi-discrete equation the vector of state variables is given by

$$\vec{Q} = \begin{Bmatrix} \rho_1\phi_1 \\ \rho_2\phi_2 \\ \rho\vec{V} \\ E \\ \phi_1 \end{Bmatrix}, \tag{2.22}$$

the grid spacings by Δx, Δy, and Δz, where $\Delta x = x_{i+1/2} - x_{i-1/2}$ and similar for y and z. The cell fluxes are given by $\vec{f}$, $\vec{g}$ and $\vec{h}$ for the x, y, and z normal cell faces respectively consisting of conservative convective and viscous fluxes

$$\vec{f} = \vec{f}^c + \vec{f}^v, \tag{2.23}$$

and the source terms given by $\vec{S}$.

The conservative convective flux is computed utilizing the HLLC Riemann solver [73, 74] with modifications for surface tension and the given two-fluid model [20]. The left and right states given to the Riemann solver are reconstructed using the Monotonic Upstream-Centered Scheme for Conservation Laws (MUSCL) [37] on the primitive variables for all computational cells utilizing a minmod limiter.

A tangent of hyperbola interface capturing scheme, ρ-THINC, is utilized [19] replacing the MUSCL reconstruction scheme for the volume fraction and phasic densities at the

interface. The reconstruction scheme assumes a hyperbolic tangent profile in cells contain the fluid interface for the volume fraction and phasic densities [54]

$$\phi_i(X) = \frac{1}{2}\left(1 + \tanh(\beta_i(\sigma_i X + x_{ic}))\right) \text{for} X \in [0,1]. \tag{2.24}$$

The center of the interface is given by x_i, X is the distance from the lower cell face normalized by the local cell length, Δx, and $\sigma_i = \pm 1$ specifies the sign of the volume fraction gradient. The thickness of the interface is weighted by the local interface orientation and a parameter to specify slope through β [79]:

$$\beta_i = \beta|n_{x,i}| + 0.01. \tag{2.25}$$

Then if

$$\overline{\phi}_i = \int_0^1 \phi_i(X)dX, \tag{2.26}$$

is required [54] the interface center for the cell can be uniquely determined and Eq. 2.24 can be solved for $\phi_i(X)$ to determine the left and right states. Making a similar assumption for the phasic densities [19]

$$(\overline{\rho_1\phi_1})_i = \rho_1 \int_0^1 \phi_{1,i}(X)dX \tag{2.27}$$

$$(\overline{\rho_2\phi_2})_i = \rho_2 \int_0^1 \phi_{2,i}(X)dX, \tag{2.28}$$

allows for a solution for ϕ_1 and ϕ_2. This can then be used in conjunction with Eq. 2.24 to reconstruct the values at the cell faces

$$(\rho_1\phi_1)^R_{i-1/2} = \frac{4\sigma_i\beta_i(\overline{\rho_1\phi_1})_i}{A + 2\sigma_i\beta_i}\phi_i(X=0) \tag{2.29}$$

$$(\rho_2\phi_2)^R_{i-1/2} = \frac{4\sigma_i\beta_i(\overline{\rho_2\phi_2})_i}{A - 2\sigma_i\beta_i}(1 - \phi_i(X=0)), \tag{2.30}$$

where

$$A = \ln\left(\frac{(\exp(2\sigma_i\beta_i)\exp(2\beta_i x_{ic})+1)^2}{\exp(2\sigma_i\beta_i)(\exp(2\beta_i x_{ic})+1)^2}\right), \tag{2.31}$$

and similarly for the left states at $i+1/2$ with $X=1$.

Reconstruction is applied for any cell in which $\epsilon < \phi_1 \leq 1-\epsilon$ where epsilon is specified as $\epsilon = 10^{-5}$. In addition, the requirement that $(\phi_{i+1}-\phi_i)(\phi_i-\phi_{i-1}) > 0$ is applied as a monotonicity constraint. This approaches follows that of Shyue and Xiao [70] and is applied on a dimension by dimension basis [19].

To calculate the viscous fluxes the approach Coralic and Colonius [9] is followed. For consistency the velocities obtained as the solution to the Riemann problem at the face are utilized

$$\frac{\partial \vec{V}_{i,j,k}}{\partial x} = \frac{\vec{V}_{i+1/2,j,k} - \vec{V}_{i-1/2,j,k}}{\Delta x}. \tag{2.32}$$

The velocity gradients at the face are then computed

$$\nabla\vec{V} = \frac{1}{2}((\nabla\vec{V})_L + (\nabla\vec{V})_R). \tag{2.33}$$

The viscous fluxes are then calculated at each face utilizing these values in the computation of the viscous stress tensor.

The scheme is moved forward in time using the third order, total variation diminishing (TVD) Runge-Kutta scheme [21]

$$\vec{Q}^{(1)} = \vec{Q}^n + \Delta t L(\vec{Q}^n) \tag{2.34}$$

$$\vec{Q}^{(2)} = \frac{3}{4}\vec{Q}^n + \frac{1}{4}\left(\vec{Q}^{(1)} + \Delta t L(\vec{Q}^{(1)})\right) \tag{2.35}$$

$$\vec{Q}^{n+1} = \frac{1}{3}\vec{Q}^n + \frac{2}{3}\left(\vec{Q}^{(2)} + \Delta t L(\vec{Q}^{(2)})\right) \tag{2.36}$$

with the right hand side of Eq. 2.21 represented by $L(\vec{Q})$.

CHAPTER 3. SOLVER DEVELOPMENT

This chapter discusses some of the improvements made to the computational solver to enable the solution of problems of interest. In particular rectilinear grids are added to reduce computational expense and parallelization completed to utilize additional computational resources. A turbulent inflow condition is also added.

3.1 Rectilinear Grids

To efficiently make use of computational resources and focus computational effort on regions of interest the solver is modified to utilize rectilinear, or stretched, grids and a grid generation routine is created to generate suitable grids. An example of such a grid is shown in Fig. 3.1, where it is used in a preliminary simulation of a liquid jet in subsonic crossflow.

The grid spacing in each direction is broken up into an arbitrary number of layers or regions where grid spacing can be specified on a dimension by dimension basis so as to best capture the flow physics of interest. In each layer the spacing and stretching ratios can be controlled, while cell sizes at the adjoining regions are matched to prevent abrupt changes in grid spacing. Combined these features provide for the creation of grids that can be efficiently tailored to capture flow physics while reducing overall computational requirements. This results in a large savings in computational cost, especially in 3 dimensions. In the case presented in Fig. 3.1 the stretched grid yields a reduction in cell count of over 70% compared to a corresponding uniform grid–leading to a similar

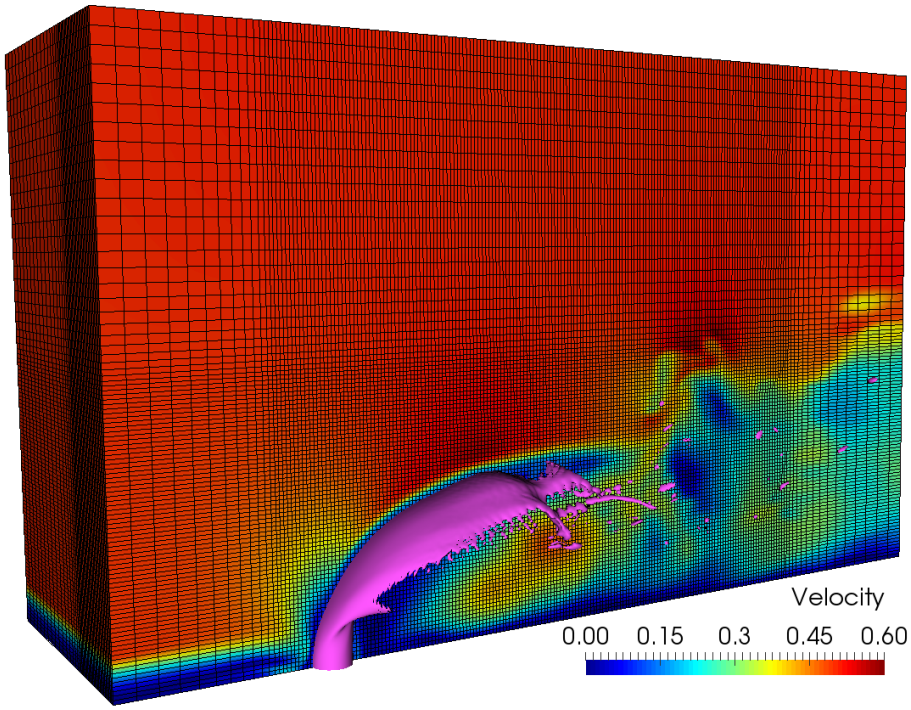

Figure 3.1 Example of a 3 dimensional rectilinear grid used in preliminary simulations of a liquid jet in crossflow; only every other grid point is plotted.

reduction in computational cost. This is a reduction from 24 million grid cells to 6.2 million cells. While this level of computational savings in not possible for all problems, the savings in computational cost is significant across a number of the cases investigated.

3.2 Parallelization

Given the size of the problems to be considered–on the order of 100 million cells–in order to be able to solve the problems in a reasonable amount of time the use of parallel resources is necessary. Given the nature of the available computational resources distributed memory parallelization is necessary. To this end, the code is parallelized utilizing Message Passing Interface (MPI) [15] to enable the use of large clusters of distributed resources.

In a parallel MPI implementation every processor independently runs the application and message passing or communication between processors only occurs when specifically implemented through MPI function calls. The conversion of a serial explicit flow solver–especially one employing ghost cells for imposing boundary conditions–to parallel is a relatively straightforward procedure. For the approach utilized here communications are only needed to update the ghost cells and adjust time step size to enforce the CFL condition.

Ghost cells are additional cells that are added at the edge of the domain and used to enforce a proscribed boundary condition. Before each time or sub-time step the values in these cell are updated to apply the specified boundary condition. Fluxes are then computed on the interior to the domain utilizing the ghost cells to enforce the boundary conditions without modification to the local stencil. The solution is then advanced utilizing the computed fluxes and the ghost cells are updated prior to beginning the next iteration.

To parallelize the solver, the solution domain is decomposed into individual processor grids. An example of a 2 dimensional decomposition is presented in Fig. 3.2. After decomposing the domain each grid contains one part of the solution domain with ghost cells surrounding each individual domain. The numbers represent the process number associated with each sub grid and the ghost cells are shown by the area between the solid and dash boxes as shown for process zero. The ghost cells overlap with the neighboring computational domain for the interior boundaries. In this approach each grid proceeds in an identical fashion as a serial approach with the exception of boundary condition enforcement.

The exterior, true boundary, ghost cells are updated in a similar fashion as a serial approach to enforce the specified boundary conditions. The interior ghost cells are updated to store the relevant solution data from neighboring processors which become the boundary conditions for these cells. As previously mentioned, at the completion of every

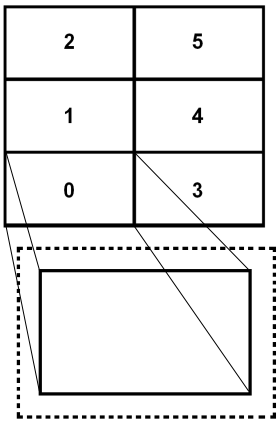

Figure 3.2 Example 2 dimensional domain decomposition.

sub time step the boundary conditions are updated at which point the interior processor grids pass the relevant solution data to the neighboring processors which is stored in the ghost cells.

The time step size must also be properly treated to satisfy the stability criterion. The maximum wave speed is computed on each of the individual processor grids at the beginning of each time step. Then an MPI function call is used to reduce the maximum value on each grid to the global value. This value is used to adjust the time step size if necessary and the new time step size is broadcast to each processor.

The strong scaling performance is investigated after completing the MPI implementation. To assess the performance both the speed-up and efficiency of the scaling is explored. The speed up relative to the reference cases is presented where the speed-up is defined [22]

$$\text{Speed-up} = \frac{\text{Total Time for Reference Case}}{\text{Total Time}}, \tag{3.1}$$

and efficiency [51]

$$\text{Efficiency} = \frac{\text{Speed-up}}{\text{Number of Nodes / Reference Number of Nodes}}. \tag{3.2}$$

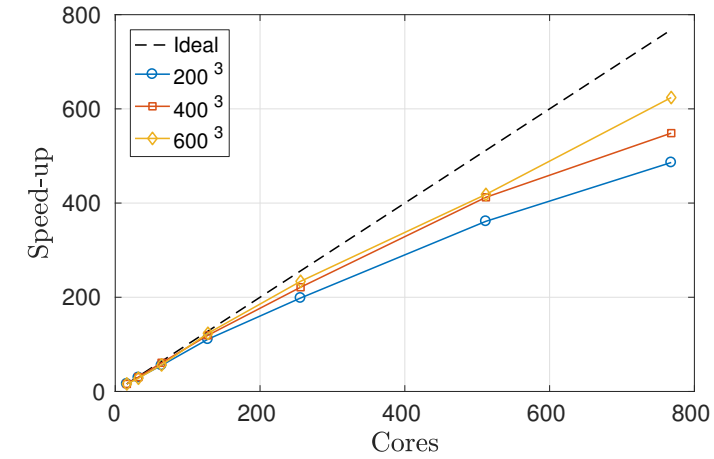

(a) Condo

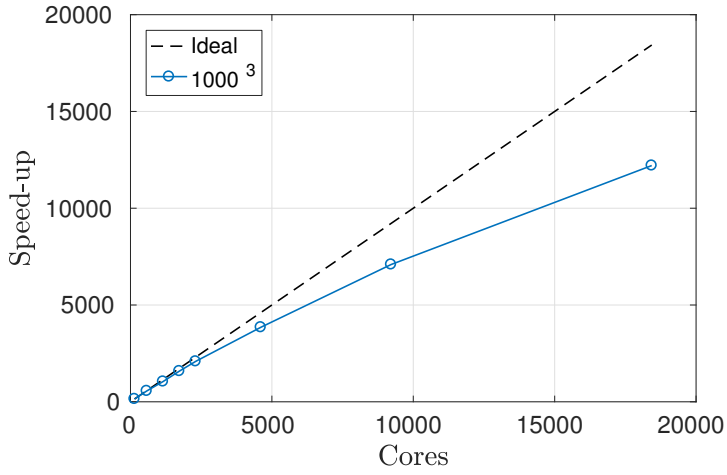

(b) Thunder

Figure 3.3 Strong scaling performance of method implementation at various grid sizes on (a) Iowa State's Condo cluster and (b) AFRL's Thunder cluster.

Tests are run on two different clusters at varying grid resolutions and the results are presented in Fig. 3.3 Condo is a cluster hosted at Iowa State University and consists of two 2.6 GHz 8-core Intel E5-2640v3 cpu's for a total of 16 cores per node. It has 188 total nodes with 40 gigabit InfiniBand interconnects for internode communications. Thunder is a cluster hosted by the Air Force Research Laboratory (AFRL) at Wright-Patterson Air Force Base. It consists of two 2.3 GHz 18-core Intel E5-2699v3 cpu's for a total of 36 cores per node. Combined it has 3216 standard memory nodes with 56 gigabit InfiniBand interconnects resulting in over 100,000 cores. The reference case for Condo

is one node, while the Thunder reference case required a four node reference case due to memory requirements for the grid and available memory.

The simulations on Condo are run from core counts from 16 to 768 and from 144 to 18,432 on Thunder at the fixed overall grid sizes listed. Good scaling across all of the cases is seen with efficiencies of greater than 80% for the largest grid size on Condo. On Thunder an efficiency of greater than 75% is seen utilizing 9216 cores and 65% at the largest core count of 18,432 using 512 nodes. Overall good scaling is seen considering the large core counts explored here. The efficient scaling allows for the use of large core counts for simulations that will be necessary for the problems of interest.

3.3 Turbulent Inflow

To investigate the effects of turbulent liquid inflow on the primary atomization of liquid jets in supersonic crossflow the ability to add turbulent fluctuations to the jet inflow are necessary. The addition of turbulent fluctuations can be accomplished in a number of ways [10]. Precursor simulations can be run but they add additional cost to the overall computation solely to obtain the inflow conditions [46, 81]. Recycling methods can also be used where the data is extracted downstream of the inlet and then recycled after rescaling to enforce the inlet conditions [46, 62, 75, 82]. This however requires simulation of the inlet sufficiently far upstream such that recycling can be applied in an equilibrium region [32]. Another option is using a synthetic turbulence generation technique [33, 34, 71, 72]. These techniques are often relatively cheap in implementation in comparison to other methods [10]. Here a Fourier Transform approach is utilized from the work of Mehrabadi et al. [49] that implements the method documented by Rogallo [61]. This approach is based off of the model spectrum given by Pope and generates isotropic homogeneous turbulence [60].

To utilize the method a Taylor Microscale Reynolds number and large eddy size are provided. The Taylor Microscale Reynolds number can be calculated from the turbulent Reynolds number [12, 60]

$$\mathrm{Re}_\lambda = \left(\frac{20}{3}\mathrm{Re}_\mathrm{L}\right)^{1/2}. \tag{3.3}$$

The turbulent Reynolds number is defined as

$$\mathrm{Re}_\mathrm{L} = \frac{k^{1/2}L}{\nu}, \tag{3.4}$$

where the turbulent kinetic energy is given by k, ν is the kinimatic viscosity ($\nu = \mu/\rho$), and L is integral length scale. Furthermore the turbulent kinetic energy is related to the turbulence intensity, $I = u'/U_j$,

$$k = \frac{1}{2}u_i u_i = \frac{3}{2}u'^{\,2} = \frac{3}{2}(IU_j)^2, \tag{3.5}$$

where U_j is the mean jet inlet velocity and u' the root mean squared of the velocity fluctuations.

The velocity fluctuations generated are then mapped to the liquid inlet as shown in Fig. 3.4. To map the velocity fluctuations time dependently the velocity is extracted form a time dependent cross-section of the generated fluctuations. At the beginning of each time step the plane is advanced at the mean jet velocity and then frozen for the duration of the time step. These fluctuations are then mapped to jet inlet and added to the mean jet velocity. This process is continued until one full length of the domain of the generated velocity fluctuations has been transversed. The start location is then randomized in the periodic box to help mitigate the effects of a regular period velocity fluctuations on the solution. The box is then again transversed one full length before repeating.

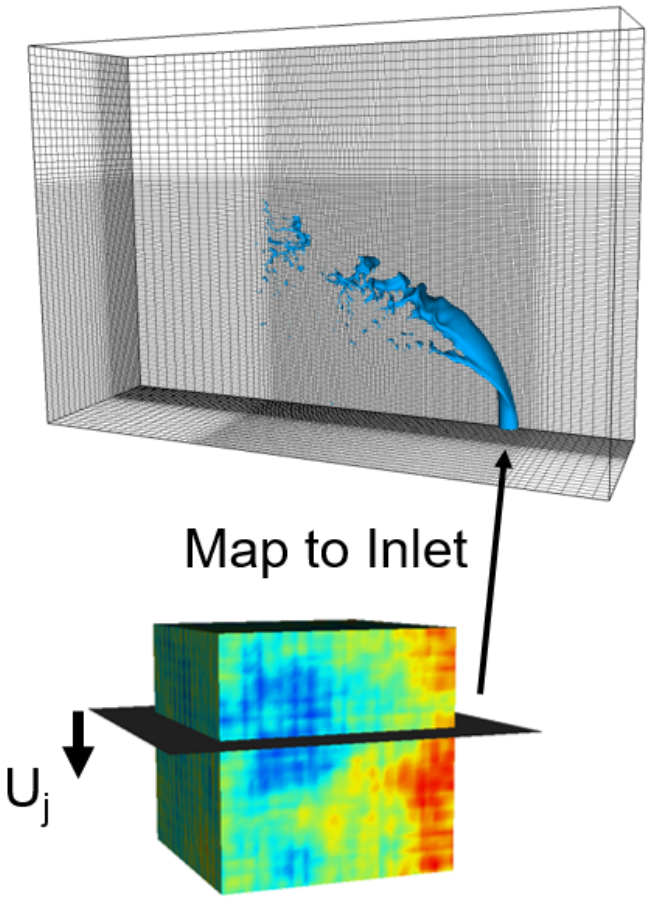

Figure 3.4 Turbulent inflow mapping to main simulation.

This approach provides a simple and computationally cheap method of generating fluctuations in the liquid inflow. Furthermore, the process develops the tools necessary in the main simulation to utilize alternative methods such as precursor simulations. The method can easily be adapted to utilize alternative databases of velocity fluctuations for the inlet domain.

CHAPTER 4. LIQUID JET IN SUBSONIC CROSSFLOW

Previous validation of the approach has shown good agreement with a variety of test cases [20]. In this chapter a validation against a more complex case of a liquid jet in subsonic crossflow is performed. The majority of results presented have been published in Hagen et al. [23].

A variety of experimental literature exists considering a wide range of conditions [4, 63, 77]. These conditions range from turbulent [36] to non-turbulent [77], pulsed injection [17], and injection at various angles to the freestream [45] at a wide variety of crossflow conditions. However, a variety of uncertainties exist that can cause difficulties when attempting to simulate and compare to a given experimental condition. In particular, results are often quite sensitive to the inflow parameters of both the liquid and gaseous crossflow as has been seen in both experiments and simulations [45, 56, 80] Furthermore, the velocity profiles of the inflows are often not fully quantified with experiments often only providing a mass flow rate or mean velocity for the liquid inflow.

The numerical simulation is designed to model the experimental results of Wu et al. [77]. A number of shadowgraph images presenting snapshots of the liquid jet atomization are provided and a number of correlations a presented including jet penetration and break-up locations. In addition, comparisons are made to the experimental work of Sallam et al. [63]. Sallam et al. provides a number of experimental correlations including the wavelengths of surface instabilities on the windward side of the jet. In addition, the experimental setup is carefully designed to reduce crossflow boundary layer development.

4.1 Simulation Conditions

The case selected is based on the experimental results of Wu et al. [77]. A liquid water jet is injected into a air crossflow and the atomization of the liquid jet is observed. The simulation parameters are presented in Table 4.1.

Table 4.1 Subsonic validation simulation parameters

Simulation Parameter	**Value**
Mach Number	0.21
$\mathrm{Re}_{\mathrm{cf}}$	6760
$\mathrm{We}_{\mathrm{cf}}$	139
Re_a	31817
We_a	3087
ϵ	566
q	9.4
N	47

The crossflow velocity is 70.9 m/s resulting in a Mach number of 0.21. This results in crossflow Reynolds and Weber numbers of 6760 and 139 respectively. The momentum flux ratio,

$$q = \frac{\rho_{\mathrm{jet}} u_{\mathrm{jet}}^2}{\rho_\infty u_\infty^2}, \tag{4.1}$$

is 9.4. The liquid and gas densities are 996 $\mathrm{kg \cdot m^{-3}}$ and 1.76 $\mathrm{kg \cdot m^{-3}}$ respectively resulting in a density ratio, ϵ, of 566. In addition, the pressure in the test section is sustained at 140 kPa.

The liquid jet is injected into a uniform velocity crossflow at t=0. The jet has a uniform constant velocity profile and is injected through a nozzle with a non-dimensional diameter D=1.0. This values corresponds to the 1.0 mm diameter used in the experiment. To model the liquid, the stiffened gas equation of state parameters are taken as $\gamma_1 = 4.4$ and $\pi_{\infty,1} = 6 \times 10^8$ Pa. The gaseous phase, air, is modeled with $\gamma_2 = 1.4$ and $\pi_{\infty,2} = 0$.

The rectangular computational domain extended from (-6.0D, 0.0D, 0.0D) to (22.0D, 8.0D, 19.0D) resulting in a rectangular prism of 28mm × 8mm × 19mm. The x axis is

aligned with the gas crossflow direction with the y and z axes aligned with the transverse direction and the vertical jet injection direction respectively. The jet is injected centered at the origin, (0.0D, 0.0D, 0.0D), and extended in radial direction with a radius of 0.5D. Around the jet a uniform grid is utilized extending from (-1.0D, 0.0D, 0.0D) to (13.0D, 2.5D, 12.0D). In the uniform region a grid resolution of $\Delta x = \Delta y = \Delta z = D/64$ is employed. In the remainder of the domain gradual stretching is utilized to the computational domain boundaries to decrease the computational expense of the simulation. The resulting grid consists of over 273 million computational cells and is shown in Fig. 4.1 where only every 8th grid point is plotted. In addition a grid with half the resolution $\Delta x = \Delta y = \Delta z = D/32$ is also simulated to compare the liquid jet trajectory at the two resolutions.

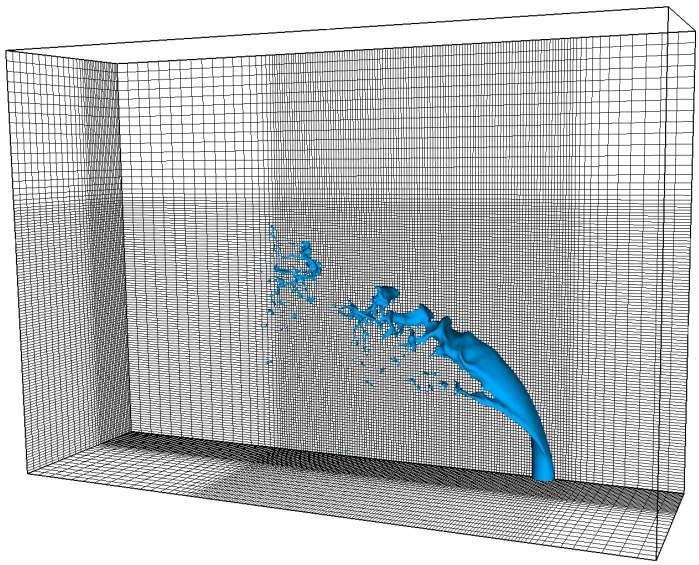

Figure 4.1 Liquid jet in subsonic crossflow computational domain; every 8th grid point is plotted.

On the lower wall a no-slip boundary condition is applied. For the z-max and y-max boundaries an extrapolation boundary condition is utilized. To reduce computational expense a symmetry boundary condition is used at the y-min boundary, the jet centerline. Finally, at x-min and x-max the boundaries are modeled as subsonic inflow and outflows.

Using the Air Force Research Laboratory supercomputer Thunder the simulation was run for 135 hours using 4608 cores to time $t = 1000$ resulting in a dimensional time $t^* = 3.0$ ms.

4.2 Results

A time history to the simulation is shown in Fig. 4.2 where every non-dimensional time interval of 100 is plotted. The velocity magnitude is plotted as a contour on the

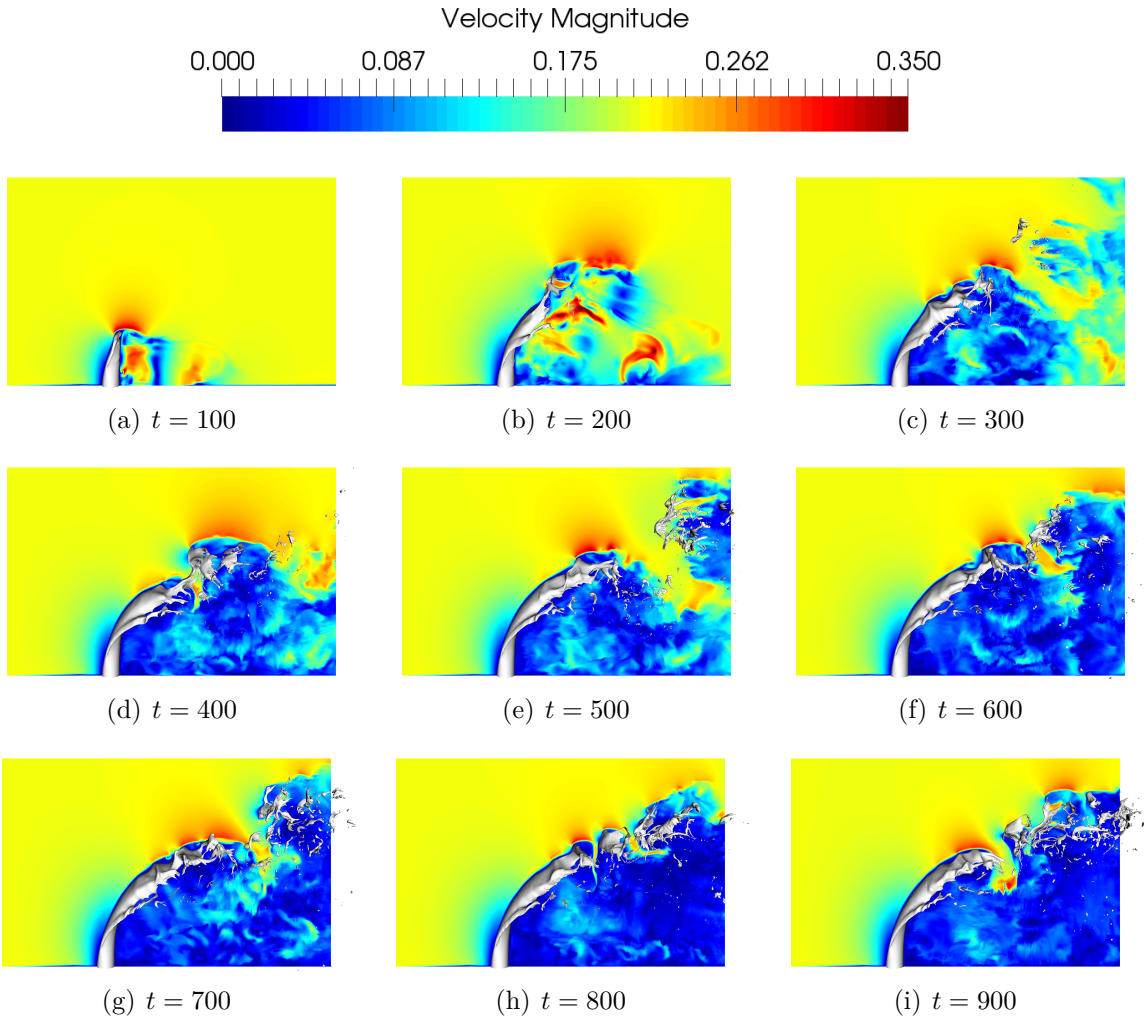

(a) $t = 100$ (b) $t = 200$ (c) $t = 300$

(d) $t = 400$ (e) $t = 500$ (f) $t = 600$

(g) $t = 700$ (h) $t = 800$ (i) $t = 900$

Figure 4.2 Subsonic simulation time history with the centerline velocity contour and the gas-liquid interface isosurface, $\phi = 0.5$, plotted.

centerline of liquid jet where the crossflow is from left to right. The gas-liquid interface is also plotted and reflected over the centerline where then interface is given by $\phi = 0.5$.

During the first moments (a)-(b) the jet is injected into the domain and the aerodynamic forces begin to affect the jet. The jet is bent rearwards and the liquid begins to shed a few drops and ligaments from the main column. By $t = 300$ instabilities on the windward surface of the jet begin to develop as more liquid is shed from the column. In addition, a low velocity wake region behind the jet is seen to developing. During the next intervals the wake region continues to develop and ligaments and drops continue shedding at intervals. Around $t = 500$ the jet trajectory begins to stabilize and the shedding of liquid becomes more regular. In addition, an interesting interaction between the velocity and the liquid column breakup is seen. High velocity regions appear to quickly push through the areas where the liquid column breaks up. This results in streaks of relatively high velocity gas appearing between packets of liquid. This pattern continues through the remaining of the simulation until the final time.

The gas-liquid isosurface at the final time is presented in Fig. 4.3. Along the windward side of the column regular instability wavelengths are seen. These wavelengths eventually give way to the breakup of the liquid column in ligaments and droplets. These then continue to breakup up cascading to smaller features. In addition a secondary extension can be seen on the side of the liquid jet breaking up early from the column and following a slightly different trajectory. This also breaks up into ligaments and droplets similar to the main column.

Comparing to the result of Wu et al. [77] a number of similar features are seen. As in the experiment, the appearance of regular wavelengths on the windward surface are present. In addition, the pattern of shedding of the large scale features is visible which continue to breakup to smaller ligaments and droplets. However, the overall trajectory of the liquid jet does appear to show some differences between the simulation and experiment. Furthermore, a number of small scale features are absent from the

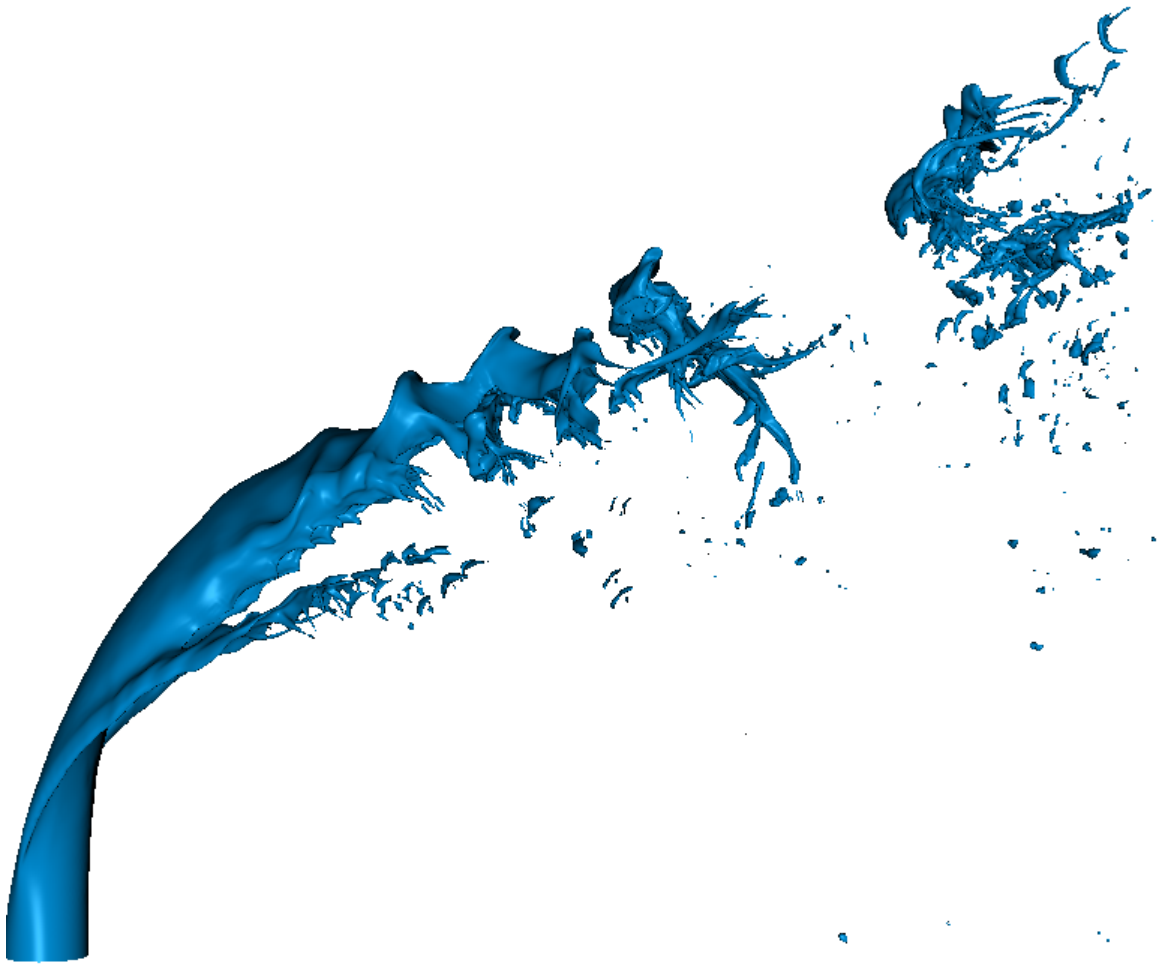

(a) left

(b) top

Figure 4.3 Liquid jet isosurface $\phi = 0.5$ at the final time $t = 1000$.

simulation. The absence of the smallest scales is an issue of available grid resolution. Although ideally a higher resolution case would be simulated to address this, the given computational cost is not currently feasible given the available resources. However, the large scale features are still observed to be reasonably captured. Overall the simulation shows good qualitative agreement with the experimental results of Wu et al. [77].

To quantitatively investigate the simulations results are compared to a number of different experimental measurements. First, the trajectory of the liquid jet is compared to the experimental results of Wu et al. [77]. The trajectory of of jet is extracted following a similar approach to Wu at a number of times. The liquid jet is extracted from the simulation ($\phi_1 \geq 0.5$) to obtain the trajectory. The windward surface is then identified along the jet at a number of times. The results of the simulations at two resolutions are shown in Fig. 4.4 where they are compared to a selection of points form Wu et al. [77]. In addition, the correlation obtained by Wu is also presented.

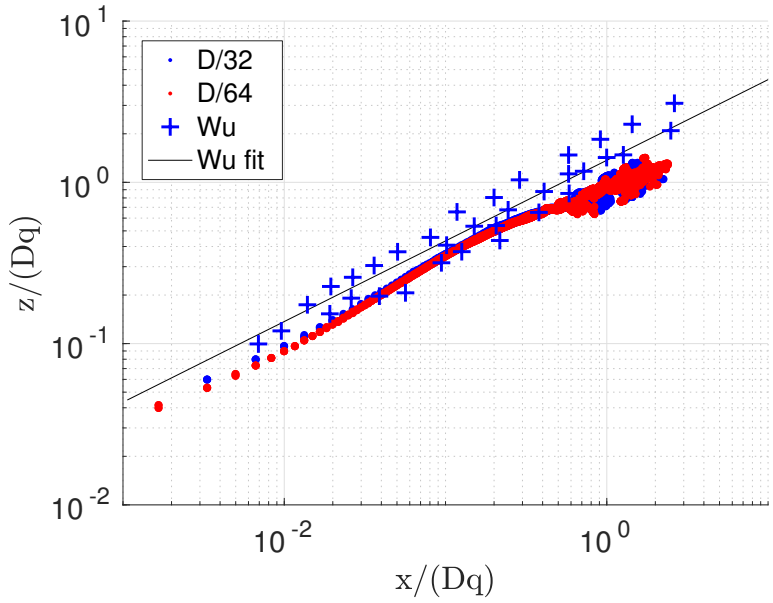

Figure 4.4 Liquid jet trajectory obtained from the simulation compared to the experimental results of Wu et al. [77].

The two grid resolutions show good agreement predicting the liquid jet trajectory throughout. Only minimal differences are seen between the two trajectories. The trajec-

tory shows good overall agreement with the experimental results throughout the liquid path. However, the penetration of the jet is noted to be slightly less than the experimental results. The systematic nature of the reduced jet trajectory in comparison to the experimental results suggests that a systematic source of error, perhaps a boundary layer, might be absent from the simulation.

The fracture location of the liquid column vertically and downstream is another frequently quantified property of liquid jets. The downstream breakup distance is measured along the x axis from the windward size of the jet at the injection location to the fracture location while the vertical breakup location is measured from the injection location to the breakup location along the z axis. Measurements at multiple times are taken and averaged for a mean breakup location of the liquid column due to the unsteady nature of the breakup location.

The vertical breakup location is presented in Fig. 4.5 where it is compared to the experimental values. It is observed, not unexpectedly, that similar conclusions to those obtained from the trajectory are seen. A slightly shorter breakup height is seen than

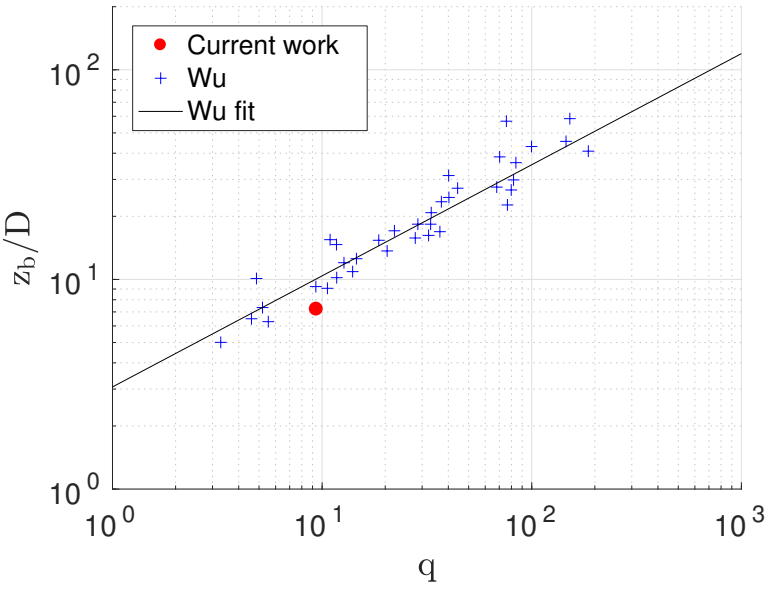

Figure 4.5 Height of the liquid column breakup location obtained in comparison to Wu et al. [77].

observed in the experimental results. The penetration height seems likely to be effected by the lack of boundary layer in the simulation when compared to the experimental results.

As such, the results of Sallam et al. [63] are used for additional comparison. In the experiments of Sallam et al. particular care is taken reduce boundary layer development in the gas crossflow in attempt to reduce uncertainties related to boundary layer effects. The simulation result is compared to the experimental data of Sallam et al. in Fig. 4.6. The ordinate in Fig. 4.6 is an empirical constant, $t_b/t^* = C_{zb}$, that is directly proportional

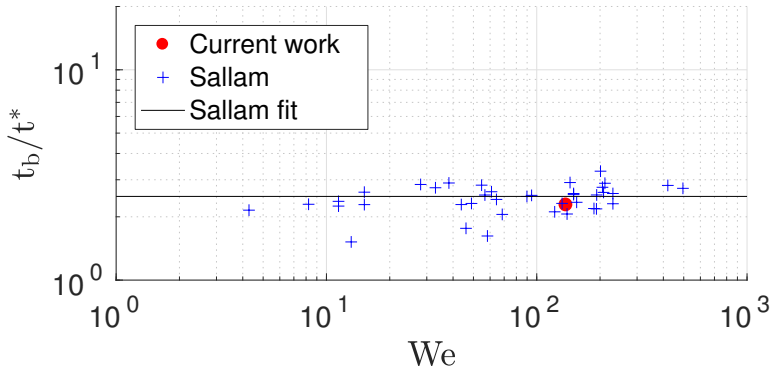

Figure 4.6 Simulated liquid column breakup time plotted against the experimental data of Sallam [63] for liquid jets in crossflow.

to the breakup distance, z_b, of the jet in the vertical direction. Here t^* and t_b are defined as [53, 63]

$$t^* = \epsilon^{\frac{1}{2}} D/u_\infty \tag{4.2}$$

and

$$t_b = z_b/u_{jet}. \tag{4.3}$$

Then, substituting into the breakup coefficient equation

$$C_{zb} = \frac{t_b}{t^*} = \frac{z_b/u_{jet}}{\epsilon^{\frac{1}{2}} D/u_\infty} = \frac{z_b}{D}\, q^{-\frac{1}{2}}, \tag{4.4}$$

a relationship for z_b is obtained. Compared to the experimental results of Sallam good agreement with the simulation is seen with the obtained value which is well within the range of experimental values obtained and lies close to the obtained fit. The empirical breakup constant, C_{zb}, is reported to be 2.5 by Sallam with and uncertainty of 7% at a 95% confidence level. This value is in agreement with the results of Lee [36] where a value of 2.44 is reported at the same confidence interval at an uncertainty of 8%. A value of 2.34 is obtained from the simulation which agrees well with these results. In both of these cases boundary layer development is minimized during the experimental testing likely leading to the better agreement with the simulated values. The value obtain by Wu et al. for comparison is 3.44 overall for all of the liquids tested and 3.6 for water specifically. These differences suggest that the boundary layer quantification is important and likely has an impact on liquid jet trajectory as mentioned by Mazallon et al. [48] and Osta et al. [55].

Considering this result, returning the trajectory the simulation results are plotted against the fit obtained by Sallam et al. in Fig. 4.7 for the trajectory of liquid of a jet in the shear breakup regime ($We_{cf} > 110$). Significantly better agreement is observed comparing to these results than the previous comparison to the data of Wu et al.

Returning to the fracture location, the downstream breakup location, x_b, is also measured as previously discussed. The breakup length obtained in the simulation is plotted against the results of Wu et al. [77] as shown in Fig. 4.8. The simulated value of the column fracture location agrees well with the spread of data in Wu et al. as shown. In addition the results are also observed to agree well with the findings of Sallam et al. [63] who reported a value of 8.0 in good agreement with the results of Wu et al.

Another quantity of significant interest is the wavelengths of the instabilities that appear on the liquid column. These wavelengths develop on the liquid column and can provide insight into the mechanisms related to primary atomization of a liquid column [63]. The wavelengths in the simulation are observed primarily on the windward

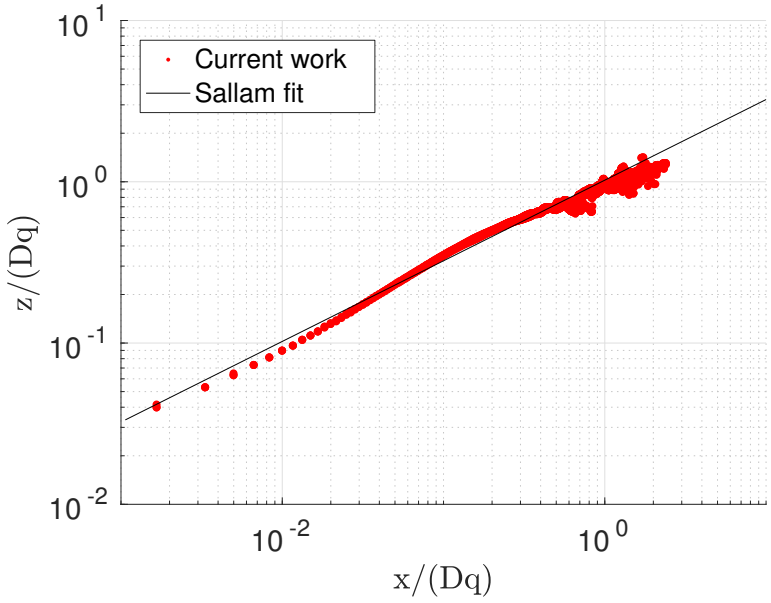

Figure 4.7 Comparison of the jet trajectory to the fit of Sallam et al. [63].

side of the jet as can be seen in figure 4.3. This feature has been observed to show a strong dependence on Weber number [63] and thus surface tension. As such, the surface instability wavelengths are a good assessment of the effects of surface tension in the simulation. To examine this, the wavelengths of the instabilities are measured where they first appear along the liquid column where as before the gas-liquid interfaces is given by $\phi = 0.5$. The wavelengths are measured at a few times and the average value is shown in Fig. 4.9 where it is compared to the experimental data of Sallam et al. [63]. As is observed the measured surface wavelengths agree fairly well with the experimental data. This suggests that the numerical approach is able to capture the effects of surface tension on the primary atomization of a transverse liquid jet.

Overall good agreement is seen with a number of experiemental parameters for this subsonic case. Some uncertanties exist due the uncertainty of the boundary layer when comparing to the results of Wu et al. [77]. However, the results of Sallam et al. [63] suggest that the effects of the boundar layer could have an impact on the liquid jet

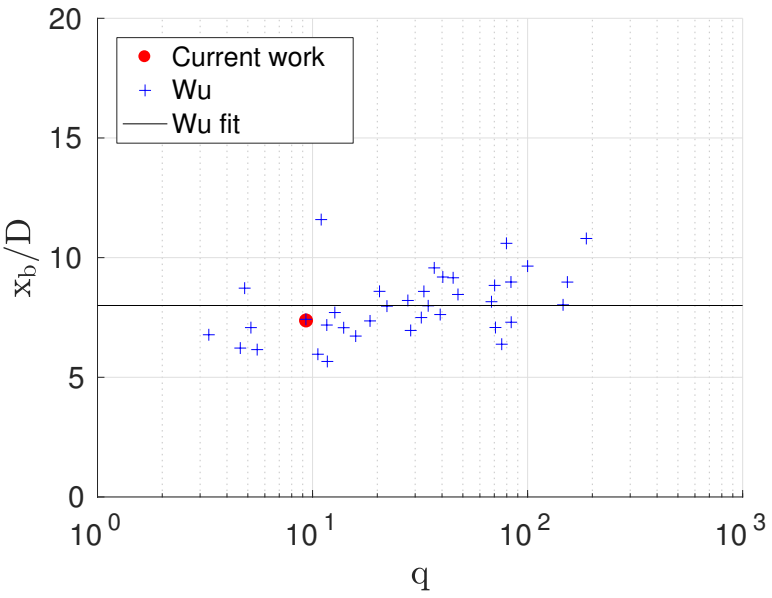

Figure 4.8 Fracture distance of the liquid column as obtained in the simulation compared to results of Wu [77].

trajectory. Comparing the entirety of the results it appears that the numerical approach is well suited to the investigation of liquid jets in crossflows.

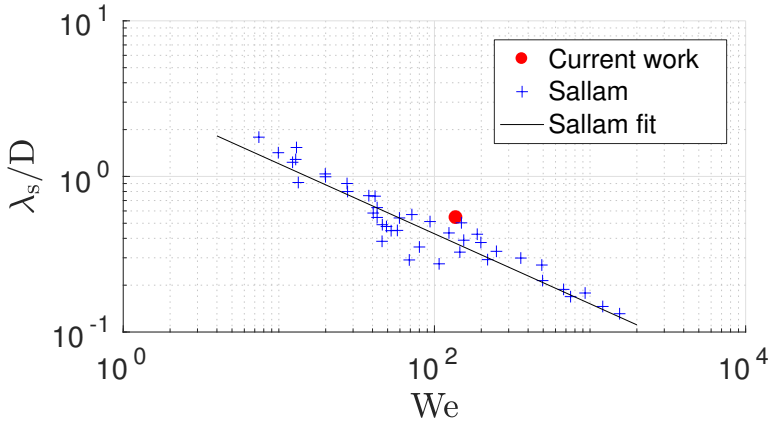

Figure 4.9 Simulated Liquid surface wavelengths compared to experimental results of Sallam [63].

CHAPTER 5. LIQUID JET IN SUPERSONIC CROSSFLOW

In this chapter a liquid jet in supersonic crossflow is considered. The simulation conditions replicate an experiment performed by Lin at the Air Force Research Laboratory. The results are compared to the experimental correlations of Lin et al. [41] and Yates [83]. The effect of turbulent inflow conditions for the liquid jet are investigated to improve comparisons to experimental data. Previous work in subsonic primary atomization has shown inflow conditions can have significant effects on the jet trajectory and breakup [36, 45, 56]. Multiple Taylor Microscale Reynolds numbers are considered as the exact inflow conditions are not specified. The resulting effects on trajectory and breakup location are investigated.

5.1 Simulation Conditions

The selected case for the supersonic simulation is based upon experiments performed by the Air Force Research Lab. A liquid water jet is injected into an air crossflow as in the subsonic case, however now the crossflow velocity is supersonic. The parameters used for the supersonic simulation are presented in Table 5.1.

In this case, the crossflow has a Mach number of 2.0 and a freestream crossflow velocity of 690 m/s. The crossflow Reynolds and Weber numbers are 11,808 and 2064 respectively due to the significant increase in crossflow velocity. An inlet velocity profile was utilized to match the inflow conditions from experimental tests. The densities of the

Table 5.1 Supersonic simulation parameters

Simulation Parameter	**Value**
Mach Number	2.0
$\mathrm{Re}_{\mathrm{cf}}$	11809
$\mathrm{We}_{\mathrm{cf}}$	2064
Re_a	5904
We_a	516
ϵ	3215
q	3.41
N	47

two fluids are 996 $\mathrm{kg} \cdot \mathrm{m}^{-3}$ and 0.31 $\mathrm{kg} \cdot \mathrm{m}^{-3}$ for the liquid and gas respectively resulting in a density ratio for the two fluids of 3215.

At $t = 0$ the liquid jet is injected into the crossflow with a nozzle having a $D = 1.0$ non-dimensional diameter. The corresponding physical value for the nozzle is 1.02 mm. Values for the stiffened gas equation of state parameters are given as before with $\gamma_1 = 4.4$, $\Pi_{\infty,1} = 6 \times 10^8$ Pa and $\gamma_2 = 1.4, \Pi_{\infty,2} = 0$ for the liquid and gas phases respectively.

The computational domain is a rectangular cuboid in the region [-10.0D, 17.0D] $\times$ [0.0D, 8.0D] $\times$ [0.0D, 14.0D] in the x, y, and z directions. An identical coordinate system as used in subsonic simulation is utilized. The jet is injected at the origin of the domain with a radius of 0.5D. A uniform grid was used in around the injection location in the region [-3.0D, 12.0D] $\times$ [0.0D, 4.0D] $\times$ [0.0D, 9.0D]. The resolution in the uniform region is given by $\Delta x = \Delta y = \Delta z = D/20$ and the grid gradually stretches outside of this area to the boundaries to reduce computational expense. Two of the cases are run at a higher grid resolution of $\Delta x = \Delta y = \Delta z = D/40$. The resulting grid is shown in Fig. 5.1.

Similar boundary conditions as in the subsonic simulation are utilized. A no-slip boundary condition is applied to the lower wall. An extrapolation boundary condition is utilized for z-max and y-max and a symmetry boundary is used at y-min. The x-min and x-max boundary conditions are modified to be supersonic inflow and outflow conditions

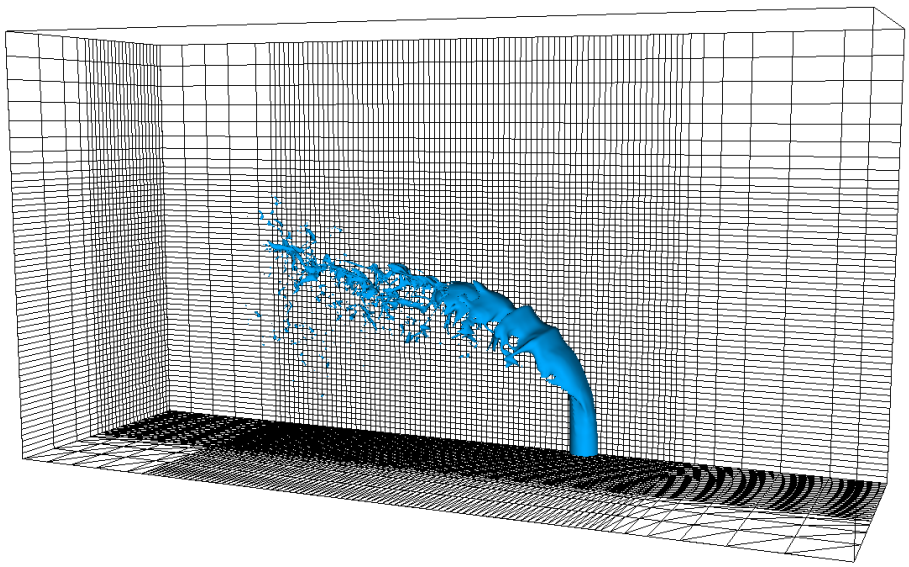

Figure 5.1 Liquid jet in supersonic crossflow computational domain only every forth grid point is plotted for the $\Delta x = D/20$ case.

as is required by the supersonic Mach number with an inlet velocity profile matching experimental data as presented in Fig. 5.2.

To explore the effect of turbulence on the liquid jet in supersonic crossflow, turbulent fluctuations are added to the uniform mean inlet velocity of 22.6 m/s. As discussed in section 3.3, homogeneous isotropic turbulent fluctuations are generated and mapped to the liquid inlet in a time dependent fashion. Two turbulent intensities of 10% and 20% are considered along with two large eddy length scales 1.0D and 0.1D. The turbulence intensities are estimated from the work of Basse who quantified turbulence intensity in the Princeton Superpipe [3]. Basse developed a relationship for the turbulence intensity averaged over the pipe area

$$I = 0.317\mathrm{Re}^{-0.110}, \tag{5.1}$$

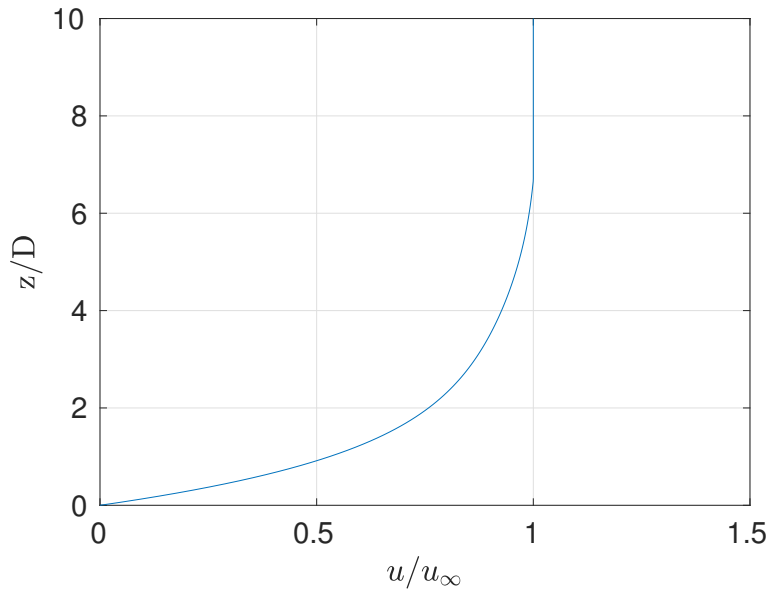

Figure 5.2 Gas inlet velocity profile used in supersonic crossflow simulation.

for a smooth pipe. The resulting turbulence intensity for given liquid Reynolds number of approximately 22,500 is then 0.105. This result leads to the selection of the values 0.1 and 0.2 to explore a range of turbulence intensities. Four turbulent liquid inflow cases are simulated as shown in Table 5.2 along with a comparison to a non-turbulent inflow case as a baseline. The individual cases will be reference using their respective Taylor

Table 5.2 Turbulent inflow conditions and Taylor Microscale Reynolds number

		Large Eddy Size	
		1.0D	**0.1D**
Intensity	**0.1**	145.4	46.0
	0.2	205.6	65.0

Microscale Reynolds number using the conditions given in the table. The effect of the turbulent fluctuations are explored here to gain an understanding of their impact on the atomization of a liquid jet in supersonic crossflow.

The simulations are until a time $t = 600$ resulting in a dimensional time of approximately $t^* = 1.75$ ms. Each simulation at a resolution of $\Delta x = D/40$ took 72 hours to run on 512 cores on the Condo cluster at Iowa State University.

5.2 Results

The results of the simulations at time intervals of $t = 150$ are presented in Fig. 5.3 where comparisons between the highest Taylor Microscale Reynolds number and the non-turbulent cases are investigated. By the first time of $t = 150$ both simulations show the liquid jet has traveled significantly into the domain. A bow shock is present in front of the injection point and a wake is developing downstream of the liquid jet. A separation region has developed upstream of the injection point. Liquid is starting to shed from the non-turbulent case while liquid drops are seen downstream in the turbulent case. Waves are developing along the windward surface of the turbulent case along with a more upright trajectory than the uniform case.

At $t = 300$ surface waves along the windward surface have developed for both cases. Comparing the breakup process a contrast is seen between the two cases. While the non-turbulent case has liquid droplets that break off the reward portion of the column relatively far downstream, large scale column breakup appears in the turbulent case with large chunks of liquid breaking from the column at semi-regular intervals. In addition, the trajectory differences at this time have become more apparent. The non-turbulent jet quickly deflects in the crossflow direction in comparison to the turbulent jet penetrates deeper into the crossflow. As a result, the wake regions also show variations between the two cases.

This difference in wake regions is also seen at $t = 450$. In the non-turbulent case the wake appears relatively well defined. In the turbulent case, a main wake region is seen behind the liquid column. Due to differences in the breakup behavior chunks of

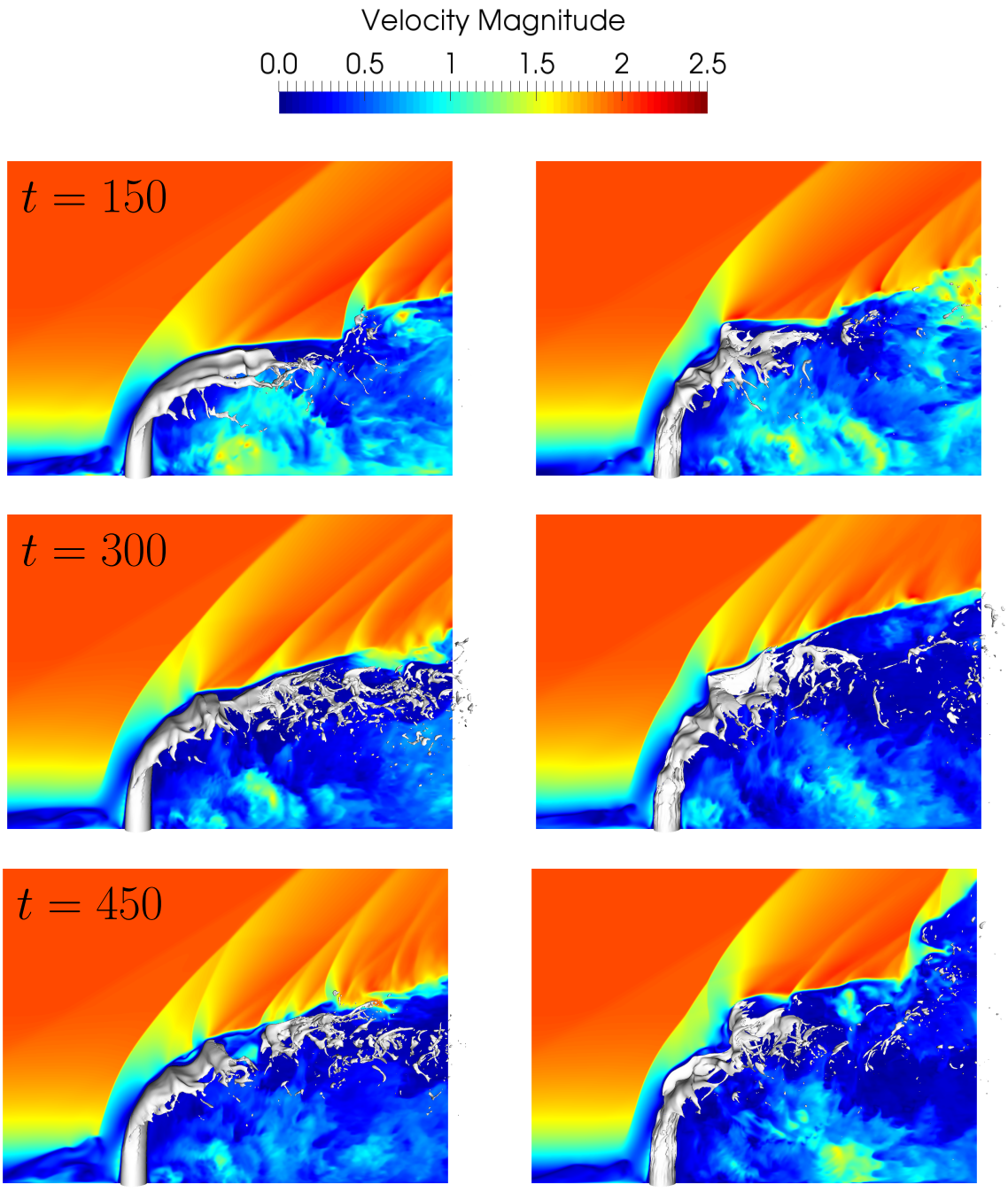

(a) Non-turbulent

(b) $\mathrm{Re}_\lambda = 206$

Figure 5.3 Supersonic simulation time history with the centerline velocity contour and the gas-liquid interface isosurface, $\phi = 0.5$, plotted for the not-turbulent and $\mathrm{Re}_\lambda = 206$ cases.

liquid are ejected into the high velocity crossflow. Ahead of each of these packets of liquid a bow shock appears and behind a wake region develops as seen in Fig. 5.4. These packets of liquid then continue to breakup in ligaments and smaller droplets as the high speed crossflow interacts with them. This results in a less well defined wake region with relatively high velocity crossflow gas entering the wake region as seen at $t = 450$ for the turbulent case.

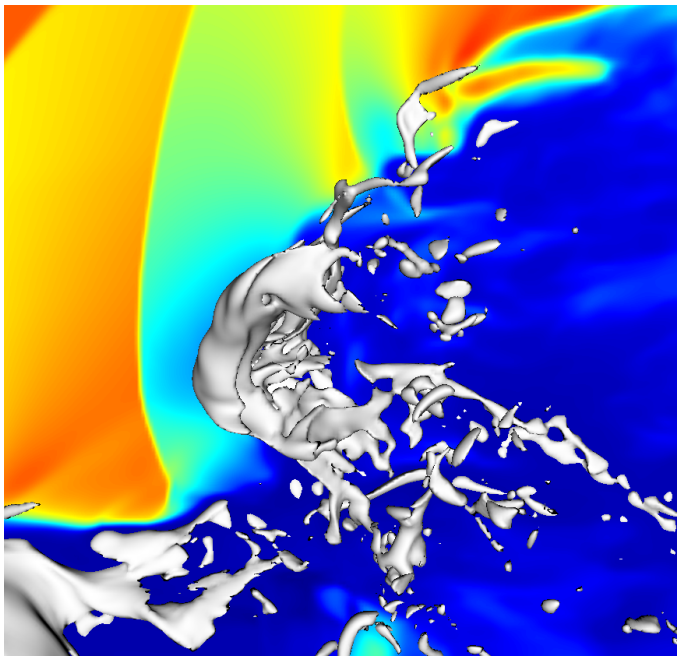

Figure 5.4 Post column breakup liquid undergoing secondary breakup with the isosurface $\phi = 0.5$ and centerline velocity magnitude.

The isosurface of the liquid at the final time of $t = 600$ is shown in Fig. 5.5 for the two cases. Significant differences between the non-turbulent and turbulent cases are observed. In particular a difference in the general breakup behavior is seen. In the turbulent case relatively large amplitude waves appear in the liquid column which then leads to column fracture. However, in the non-turbulent case these surface waves are still present, but they are of a significantly reduced amplitude. Relatively smaller features are generated initially as a result for the non-turbulent case as opposed to the larger scale of breakup observed in the turbulent case. The column fracture location appears to be

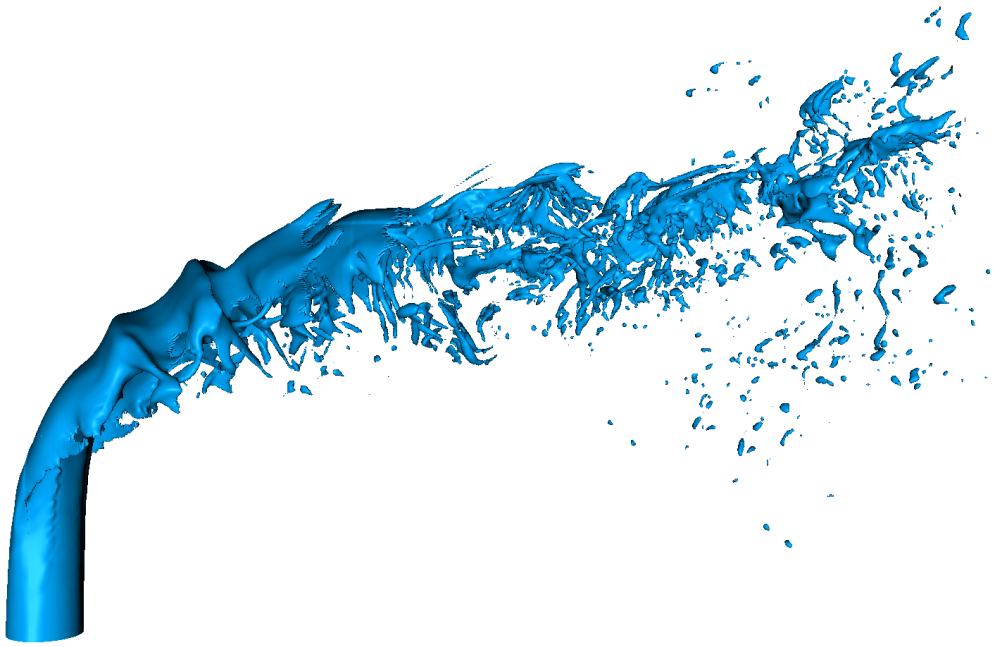

(a) Non-turbulent

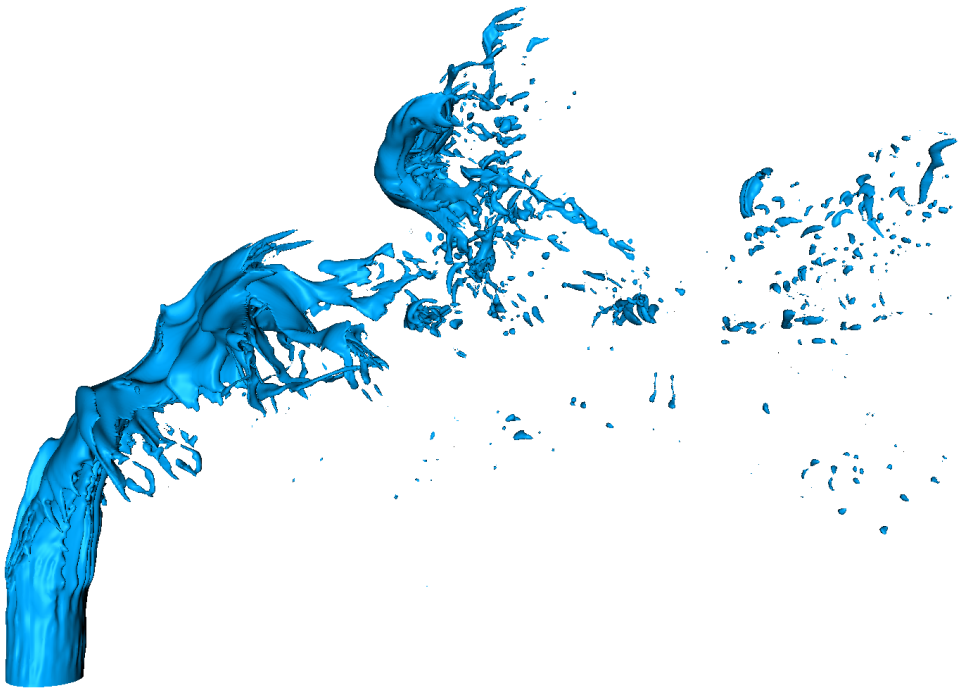

(b) $\mathrm{Re}_\lambda = 206$

Figure 5.5 Liquid jet isosurface $\phi = 0.5$ at the final time $t = 600$.

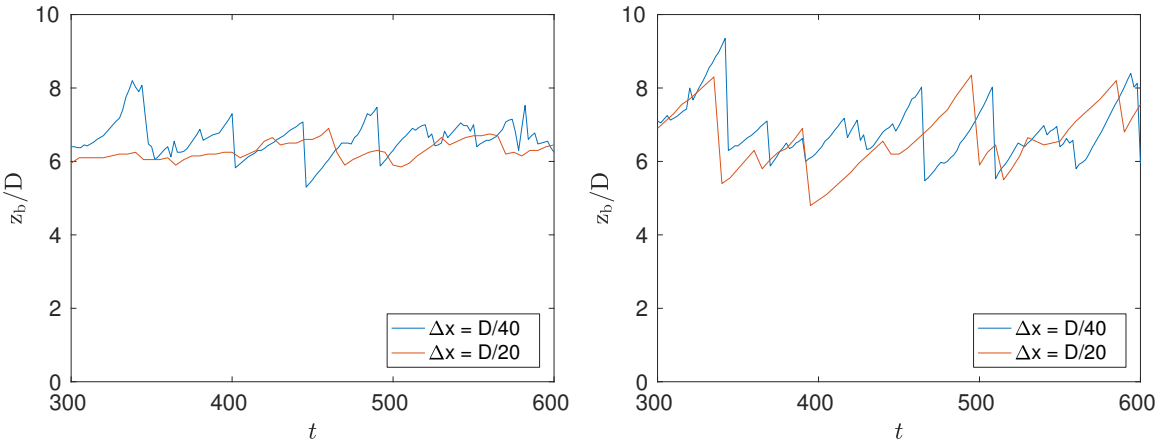

(a) Non-turbulent (b) $\mathrm{Re}_\lambda = 206$

Figure 5.6 Comparison of column fracture height during the second half of the simulation.

significantly further downstream for the non-turbulent case. Finally, greater penetration is seen in the turbulent cases as observed seen in both Fig. 5.3(b) and Fig. 5.5(b).

The time dependent column fracture location is extracted for both grid resolutions for the uniform and $\mathrm{Re}_\lambda = 206$ cases and the results for the two simulations are shown in Fig. 5.6. Relatively good average agreement is seen between the two grid resolutions for both inlet conditions. However, for the non-turbulent case larger fluctuations are present during the first portion while similar fluctuations are seen throughout the simulation for the turbulent case. These fluctuations in the non-turbulent case reduce in magnitude toward the end of the simulation. Considering this, the remainder of the results utilize the $\Delta x = D/20$ cases for comparison.

To quantitatively compare the trajectories the liquid at each x location is extracted during the last 150 non-dimensional time units and the max value plotted as shown in Fig. 5.7. The results are compared to empirical correlations as given by Eqs. 5.2 – 5.4.

$$z/D = 3.94q^{0.47}(x/D)^{0.21} \tag{5.2}$$

$$z/D = 4.73q^{0.30}(x/D)^{0.30} \tag{5.3}$$

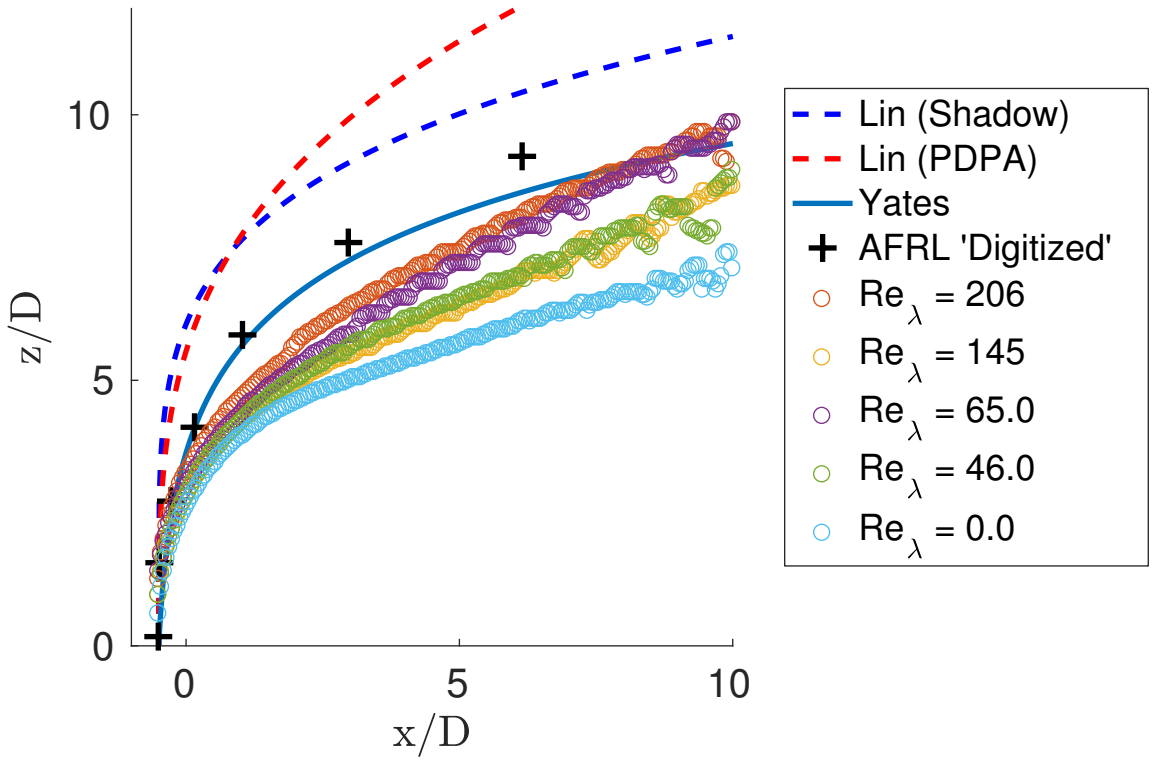

Figure 5.7 Trajectory of the liquid jet for various Re_λ compared to empirical correlations of Lin et al. [41] and Yates [83].

$$z/D = 1.1q^{0.5}\ln(1 + 10x/D) \tag{5.4}$$

Equation 5.2 is an empirical correlation developed by Lin et al. [41] using shadowgraph visualization and Eq. 5.3 is obtained from PDPA [42]. Yates et al. also developed a empirical correlation for the trajectory using direct-luminosity [83] which is given by Eq. 5.4.

Comparing the simulation results to the experimental correlations it is observed that the turbulent jets better match the experimental data. The non-turbulent jet underpredicts the trajectory in relation to the experiments, in particular the PDPA measurements of Lin et al. [42]. Overall, better agreement with the correlation of Yates is seen. However, it is unknown what the exact inflow conditions are for either correlation. In general, the jet trajectory appears to increase with an increase in the turbulence intensity of the inflow. It is noted that the turbulent inflow here is likely not truly representative

of the jet injector inflow as homogeneous isotropic turbulence is not representative of developing turbulent pipe flow. However, the simulations suggest that turbulent inflow has demonstrative effects on the liquid jet trajectory. This effect has been observed in subsonic flow [56, 78] and highlights the importance of quantifying properties of the injector exit particularly when comparisons to simulation data are desired.

Noting the apparent differences in the downstream column fracture location in Fig. 5.5 the breakup location is investigated. The breakup location is extracted at intervals

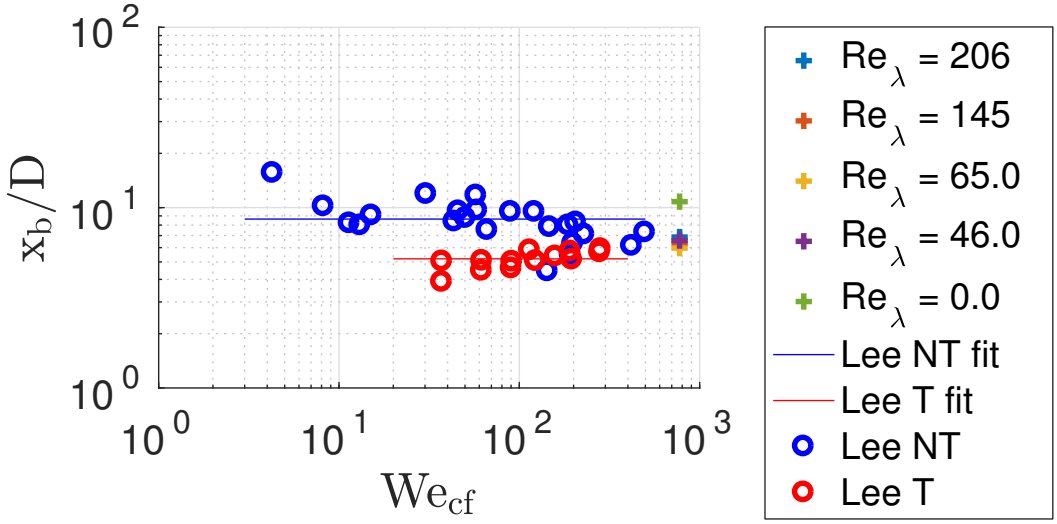

Figure 5.8 Downstream column fracture location comparison for jet in supersonic cross-flow compared to non-turbulent (NT) and turbulent (T) experimental data of Lee et al. [36].

of $\Delta t = 5$ during the second half of the simulation and then averaged. Although it has little impact in the current study, an effective Weber number is used to compare the supersonic results to the subsonic data. The effective Weber number is computed using post shock values from the normal shock jump conditions [80]

$$\mathrm{We}_{\mathrm{eff}} = \frac{2 + (\gamma - 1)M^2}{(\gamma + 1)M^2}\mathrm{We}_{\mathrm{cf}}. \tag{5.5}$$

The results are presented in Fig. 5.8 and compared to the subsonic results of Lee et al. [36]. Both the fits developed by Lee and the measured data values are compared

to the measured values in the supersonic simulations. Analyzing the results, the trend appears to be consistent with the subsonic results. All four turbulent cases exhibit a reduced downstream fracture length when compared to the non-turbulent case. Somewhat surprisingly, the column fracture distance shows decent agreement with the subsonic experimental results. The breakup location is skewed slightly down stream of the subsonic results but still lies near the values obtained by Lee et al. [36]. This is interesting considering the simulation is in a very different flow regime from the subsonic experimental results.

The breakup hight is also extracted and compared between the turbulent cases. The results are presented in Fig. 5.9 and plotted against the Taylor Microscale Reynolds number. The mean breakup height for the five cases considered here is 6.2. For the range of Reynolds numbers considered the breakup hight shows very little variation. The results suggest that although the downstream fracture length shows variation with inlet turbulence, the breakup height is relatively insensitive to jet inlet turbulence. These result differ from subsonic experiments that show a sensitively of breakup height to inflow turbulence [37]. However–as noted previously–the flow regime is significantly different than that of the subsonic jets investigated. In addition the turbulence applied to the inlet is homogeneous isotropic turbulence which may result in a different conclusion than that of a true injector which likely has a significantly different mean profile and turbulent fluctuations.

Lastly, the shock stand off distance was measured for the simulations. The detachment distance was measured 2.0D vertically from the jet injection location. At this height a shock exists upstream of the liquid jet with and incoming Mach number of approximately 1.4 as measured in the simulations. This is slightly less than the predicted value of approximately 1.5 using the inlet profile, likely due to effects of the separation region in front of the jet injection location. The results are plotted in Fig. 5.10 where they are compared to experimental data found in [40] along with the results of Xiao et

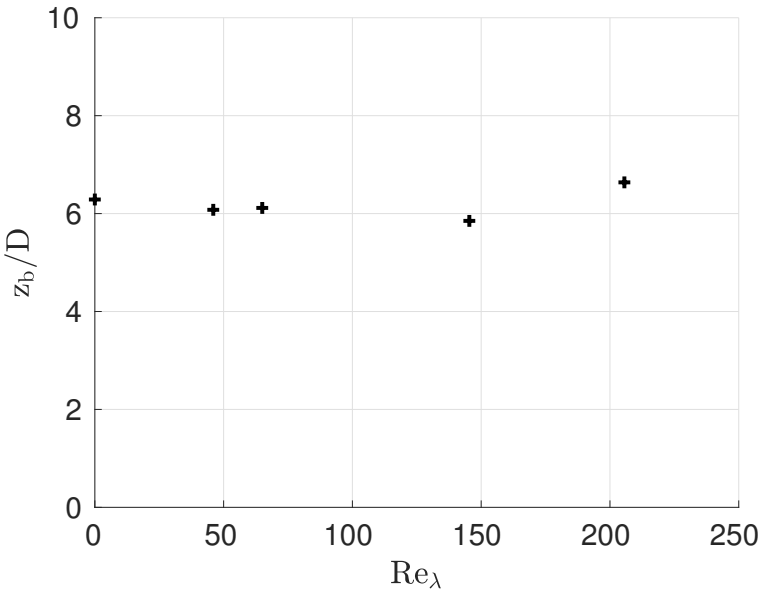

Figure 5.9 Vertical column fracture location by Taylor Microscale Reynolds number, Re_λ

al. [80]. As discussed in Xiao et al. [80], the simulated results lie between the values for a cylinder and sphere. This is logical considering while the lower portion of the jet approximately represents a cylinder, while the upper portion gives way as it is deflected by the freestream allowing the crossflow to deflect upward while still providing more overall blockage than that of flow around a sphere. Overall, the detachment distance appears to be a reasonable value. In addition, there does not appear to be any dependence on jet inlet conditions for the cases considered.

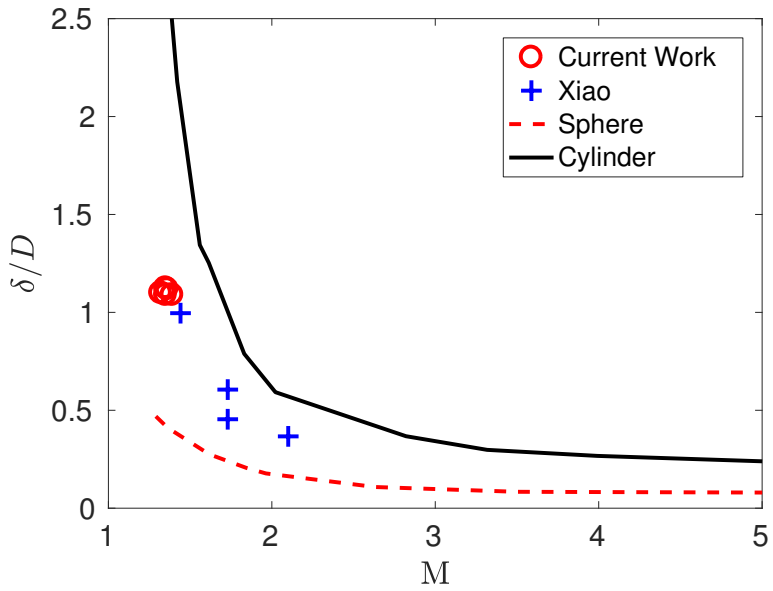

Figure 5.10 Shock standoff distance vs. Mach number compared against the results of Xiao et al. [80] and experimental data from Liepmann and Roshko [40].

CHAPTER 6. CONCLUSION AND FUTURE WORK

6.1 Conclusion

The atomization of liquid jets in crossflow have long been a topic of interest. A variety of experimental correlations have been developed for transverse liquid jets across a variety of conditions. However, experiments are often limited in their ability to observe all relevant features. Numerical simulations have the potential to provide additional insight into this complex problem, but until recently detailed numerical simulations were infeasible due to computational expense.

In this work a compressible multicomponent framework is presented that is able to solve compressible atomization problems. Modifications to the solver are completed to assist in the solution of the complex problems of interest. Rectilinear grids are added to reduce cell count and computational cost. To leverage large distributed computational resources, parallelization is implemented through the use of the Message Passing Interface. The scaling of the implementation is tested and is observed to scale efficiently to hundreds and thousands of CPU cores. In addition, a turbulent inflow boundary condition is developed using a synthetic turbulence generation method. The inflow condition is easily modifiable to enable the utilization of alternative inlet fluctuation data.

The numerical approach is validated against a liquid jet in crossflow. The results are compared to experimental correlations for trajectory, column fracture location, and surface instabilities. Good agreement is observed, although some uncertainties due to lack of boundary layer quantification are discussed. The trajectory, column fracture

location, and surface instabilities are observed to show good agreement with the results Sallam et al. [63], while the trajectory and breakup height are slightly lower than reported by Wu et al. [77].

A liquid jet in supersonic crossflow is investigated and the effect of turbulence on the liquid jet inflow and trajectory are explored. A range of turbulent inflow cases are simulated and results compared to a non-turbulent base case. A number of qualitative differences are observed between the turbulent on non-turbulent cases similar to previous results for subsonic crossflow. In general the simulations suggested an increase in jet penetration as the turbulence intensity increased. Interestingly, the downstream column breakup length agrees reasonably well with previous subsonic results. In contrast, the column fracture height appears to show little sensitivity to Taylor Microscale Reynolds number. The results suggest jet inflow conditions are important for transverse liquid jets in supersonic crossflow as has been previously discussed for subsonic crossflow conditions.

6.2 Future Work

A number of extension to the work are possible. First, a more realistic turbulent inflow for the liquid could be added to the simulation as the inflow is unlikely to be described by homogeneous isotropic turbulence. This inflow could be generated in a variety of ways as discussed in section 3.3. In particular, some options include a precursor direct numerical simulation or large eddy simulation of the injector geometry or an alternative synthetic generation method that more faithfully represents the inflow.

In addition, working with experimentalists to obtain better boundary conditions for the inlet are another possibility. The sensitivity of transverse liquid jet atomization to inflow conditions presents difficulties when attempting to compare numerical approaches to experimental results. Well defined boundary conditions could provide for better validation of numerical approaches as uncertainties from the simulations are removed.

A number of additions to the approach could also be explored, both in the physics and the numerical method. To help reduce the computational cost of the simulations multi-block meshes or adaptive mesh refinement could be explored. Adaptive mesh refinement would likely be most beneficial during the early stages of the simulation while the liquid only occupies a small percentage of the domain. The cost, however, might exceed the benefits at latter times due to the necessity of load balancing and the large percentage of the domain the liquid occupies. Additional physical models could also be added to the numerical approach. The effects of evaporation of the liquid fuel could be explored. Another option would be to explore the addition of combustion models to the numerical approach.

Lastly, the detailed simulation capabilities discussed here could be used to further the development of design based tools such as industrial computational fluid dynamics approaches. As the simulations can provide additional insights in the flow physics, they can be used to supplement experimental data in the development of reduced order simulations. In particular, the detailed simulations could be utilized to help inform breakup models or subgrid atomization models that can be used in computationally cheaper simulations.

BIBLIOGRAPHY

[1] Aalburg, C., van Leer, B., Faeth, G. M., and Sallam, K. (2005). Properties of nonturbulent round liquid jets in uniform gaseous cross flows. *Atomization and Sprays*, 15(3).

[2] Allaire, G., Clerc, S., and Kokh, S. (2002). A five-equation model for the simulation of interfaces between compressible fluids. *Journal of Computational Physics*, 181(2):577–616.

[3] Basse, N. T. (2017). Turbulence intensity and the friction factor for smooth-and rough-wall pipe flow. *Fluids*, 2(2):30.

[4] Billig, F. and Schetz, J. (1966). Penetration of gaseous jets injected into a supersonic stream. *Journal of Spacecraft and Rockets*, 3(11):1658–1665.

[5] Braconnier, B. and Nkonga, B. (2009). An all-speed relaxation scheme for interface flows with surface tension. *Journal of Computational Physics*, 228(16):5722–5739.

[6] Broumand, M. and Birouk, M. (2016). Liquid jet in a subsonic gaseous crossflow: Recent progress and remaining challenges. *Progress in Energy and Combustion Science*, 57:1–29.

[7] Chang, C.-H. and Liou, M.-S. (2007). A robust and accurate approach to computing compressible multiphase flow: Stratified flow model and ausm+-up scheme. *Journal of Computational Physics*, 225(1):840–873.

[8] Choubey, G., Pandey, K., Maji, A., and Deshamukhya, T. (2017). A brief review on the recent advances in scramjet engine. In *AIP Conference Proceedings*, volume 1859, page 020036. AIP Publishing.

[9] Coralic, V. and Colonius, T. (2014). Finite-volume weno scheme for viscous compressible multicomponent flows. *Journal of computational physics*, 274:95–121.

[10] Dhamankar, N. S., Blaisdell, G. A., and Lyrintzis, A. S. (2015). An overview of turbulent inflow boundary conditions for large eddy simulations. In *22nd AIAA Computational Fluid Dynamics Conference.(Dallas, USA, 2015)(cf. p. 55)*.

[11] Drummond, J. P., Diskin, G. S., and Cutler, A. D. (2002). Fuel-air mixing and combustion in scramjets. *38th AIAA/ASME/SAE/ASEE Joint Propulsion Confernece and Exhibit*.

[12] Durbin, P. A. and Reif, B. P. (2011). *Statistical theory and modeling for turbulent flows*. John Wiley & Sons.

[13] Faeth, G. (1991). Structure and atomization properties of dense turbulent sprays. In *Symposium (International) on Combustion*, volume 23, pages 1345–1352. Elsevier.

[14] Fechter, S. and Munz, C.-D. (2015). A discontinuous galerkin-based sharp-interface method to simulate three-dimensional compressible two-phase flow. *International Journal for Numerical Methods in Fluids*, 78(7):413–435.

[15] Forum, M. P. I. (2012). *A Message-Passing Interface Standard, Version 3.0*. University of Tennessee.

[16] Fry, R. S. (2004). A century of ramjet propulsion technology evolution. *Journal of propulsion and power*, 20(1):27–58.

[17] Fuller, R. P., Wu, P.-K., Kirkendall, K. A., and Nejad, A. S. (2000). Effects of injection angle on atomization of liquid jets in transverse airflow. *AIAA journal*, 38(1):64–72.

[18] Garrick, D. P. (2017). PhD thesis, Iowa State University, Ames, Iowa.

[19] Garrick, D. P., Hagen, W. A., and Regele, J. D. (2017a). A simple interface capturing scheme for modeling atomization in compressible flows. *Journal of Computational Physics*, 334:260–280.

[20] Garrick, D. P., Owkes, M., and Regele, J. D. (2017b). A finite-volume hllc-based scheme for compressible interfacial flows with surface tension. *Journal of Computational Physics*, 339:46–67.

[21] Gottlieb, S. and Shu, C.-W. (1998). Total variation diminishing runge-kutta schemes. *Mathematics of computation of the American Mathematical Society*, 67(221):73–85.

[22] Gropp, W., Lusk, E., and Skjellum, A. (1999). *Using MPI: portable parallel programming with the message-passing interface*, volume 1. MIT press.

[23] Hagen, W. A., Garrick, D. P., Owkes, M., and Regele, J. D. (2017). Validation of a compressible interfacial flow solver using jet in crossflow. In *29th Annual Conference on Liquid Atomization and Spray Systems*.

[24] Harlow, F. and Amsden, A. (1971). Fluid dyanmics, technical report la-4700. Technical report, Los ALamos National Laboratory, Los Alamos, NM.

[25] Heister, S. and Nguyen, T. Modeling of liquid jets injected transversely into a supersonic crossflow.

[26] Herrmann, M. (2010). Detailed numerical simulations of the primary atomization of a turbulent liquid jet in crossflow. *Journal of Engineering for Gas Turbines and Power*, 132(6):061506.

[27] Herrmann, M. (2011). The influence of density ratio on the primary atomization of a turbulent liquid jet in crossflow. *Proceedings of the Combustion Institute*, 33(2):2079–2088.

[28] Hojnacki, J. T. (1972). Ramjet engine fuel injection studies. Technical report, AIR FORCE AERO PROPULSION LAB WRIGHT-PATTERSON AFB OH.

[29] Im, K.-S., Cheong, S.-K., Liu, X., Wang, J., Lai, M.-C., Tate, M. W., Ercan, A., Renzi, M. J., Schuette, D. R., and Gruner, S. M. (2009). Interaction between supersonic disintegrating liquid jets and their shock waves. *Physical review letters*, 102(7):074501.

[30] Im, K.-S., Lin, K.-C., and Lai, M.-C. (2005). Spray atomization of liquid jet in supersonic cross flows. *AIAA paper*, 732:2005.

[31] Im, K.-S., Lin, K.-C., Lai, M.-C., and Chon, M. (2011). Breakup modeling of a liquid jet in cross flow. *International Journal of Automotive Technology*, 12(4):489–496.

[32] Keating, A., Piomelli, U., Balaras, E., and Kaltenbach, H.-J. (2004). A priori and a posteriori tests of inflow conditions for large-eddy simulation. *Physics of Fluids*, 16(12):4696–4712.

[33] Klein, M., Sadiki, A., and Janicka, J. (2003). A digital filter based generation of inflow data for spatially developing direct numerical or large eddy simulations. *Journal of computational Physics*, 186(2):652–665.

[34] Kraichnan, R. H. (1970). Diffusion by a random velocity field. *The physics of fluids*, 13(1):22–31.

[35] Kush, E. A. and Schetz, J. A. (1973). Liquid jet injection into a supersonic flow. *AIAA Journal*, 11(9):1223–1224.

[36] Lee, K., Aalburg, C., Diez, F. J., Faeth, G. M., and Sallam, K. A. (2007). Primary breakup of turbulent round liquid jets in uniform crossflows. *AIAA journal*, 45(8):1907–1916.

[37] Leer, B. V. (1977). Towards the ultimate conservative difference scheme iii. upstream-centered finite-difference schemes for ideal compressible flow. *Journal of Computational Physics*, 23(3):263–275.

[38] Li, H. and Karagozian, A. (1992). Breakup of a liquid jet in supersonic crossflow. *AIAA journal*, 30(7):1919–1921.

[39] Li, X. and Soteriou, M. C. (2016). High fidelity simulation and analysis of liquid jet atomization in a gaseous crossflow at intermediate weber numbers. *Physics of Fluids*, 28(8):082101.

[40] Liepmann, H. W. and Roshko, A. (1957). *Elements of gasdynamics*. Courier Corporation.

[41] Lin, K., Kennedy, P., and Jackson, T. (2002). Penetration heights of liquid jets in high-speed crossflows. *AIAA paper*, 873:2002.

[42] Lin, K.-C., Kennedy, P., and Jackson, T. (2004). Structures of water jets in a mach 1.94 supersonic crossflow. *AIAA paper*, 971:2004.

[43] Lin, K.-C., Laib, M.-C., Ombrelloc, T., and Carterd, C. (2017). Structures and temporal evolution of liquid jets in supersonic crossflow. In *55th AIAA Aerospace Sciences Meeting*, page 1958.

[44] Liu, H., Guo, Y., and Lin, W. (2016). Numerical simulations of transverse liquid jet to a supersonic crossflow using a pure two-fluid model. *Advances in Mechanical Engineering*, 8(1):1687814016629341.

[45] Lubarsky, E., Zinn, B., Shcherbik, D., Bibik, O., and Gopala, Y. (2012). *Fuel jet in cross flow-experimental study of spray characteristics.* INTECH Open Access Publisher.

[46] Lund, T. S., Wu, X., and Squires, K. D. (1998). Generation of turbulent inflow data for spatially-developing boundary layer simulations. *Journal of Computational Physics*, 140(2):233–258.

[47] Mashayek, A. and Ashgriz, N. (2011). Atomization of a liquid jet in a crossflow. In *Handbook of Atomization and Sprays*, pages 657–683. Springer.

[48] Mazallon, J., Dai, Z., and Faeth, G. (1999). Primary breakup of nonturbulent round liquid jets in gas crossflows. *Atomization and Sprays*, 9(3).

[49] Mehrabadi, M., Tenneti, S., Garg, R., and Subramaniam, S. (2015). Pseudo-turbulent gas-phase velocity fluctuations in homogeneous gas–solid flow: fixed particle assemblies and freely evolving suspensions. *Journal of Fluid Mechanics*, 770:210–246.

[50] Meng, J. and Colonius, T. (2015). Numerical simulations of the early stages of high-speed droplet breakup. *Shock Waves*, 25(4):399–414.

[51] Mininni, P. D., Rosenberg, D., Reddy, R., and Pouquet, A. (2011). A hybrid mpi–openmp scheme for scalable parallel pseudospectral computations for fluid turbulence. *Parallel Computing*, 37(6):316–326.

[52] Nejad, A. and Schetz, J. (1984). Effects of viscosity and surface tension on a jet plume in supersonic crossflow. *AIAA journal*, 22(4):458–459.

[53] Nicholls, J. and Ranger, A. (1969). Aerodynamic shattering of liquid drops. *Aiaa Journal*, 7(2):285–290.

[54] Nonomura, T., Kitamura, K., and Fujii, K. (2014). A simple interface sharpening technique with a hyperbolic tangent function applied to compressible two-fluid modeling. *Journal of Computational Physics*, 258:95–117.

[55] Osta, A. and Sallam, K. (2010). Nozzle-geometry effects on upwind-surface properties of turbulent liquid jets in gaseous crossflow. *Journal of Propulsion and Power*, 26(5):936.

[56] Owkes, M., Pai, M., and Desjardins, O. (2014). Large-eddy simulation study of injector geometry on liquid jet in cross-flow and validation with experiments. *52nd Aerospace Sciences Meeting*.

[57] Pai, M. G., Pitsch, H., and Desjardins, O. (2009). Detailed numerical simulations of primary atomization liquid jets in cross flow. In *47th AIAA Aerospace Sciences Meeting, Orlando, FL, January*, pages 5–8.

[58] Perigaud, G. and Saurel, R. (2005). A compressible flow model with capillary effects. *Journal of Computational Physics*, 209(1):139–178.

[59] Perurena, J. B., Asma, C., Theunissen, R., and Chazot, O. (2009). Experimental investigation of liquid jet injection into mach 6 hypersonic crossflow. *Experiments in fluids*, 46(3):403–417.

[60] Pope, S. B. (2001). *Turbulent flows*. IOP Publishing.

[61] Rogallo, R. S. (1981). Numerical experiments in homogeneous turbulence. Technical report, NASA Ames.

[62] Sagaut, P., Garnier, E., Tromeur, E., Larcheveque, L., and Labourasse, E. (2004). Turbulent inflow conditions for large-eddy simulation of compressible wall-bounded flows. *AIAA journal*, 42(3):469–477.

[63] Sallam, K. A., Aalburg, C., and Faeth, G. M. (2004). Breakup of round nonturbulent liquid jets in gaseous crossflow. *AIAA Journal*, 42(12):2529–2540.

[64] Saurel, R. and Lemetayer, O. (2001). A multiphase model for compressible flows with interfaces, shocks, detonation waves and cavitation. *Journal of Fluid Mechanics*, 431:239–271.

[65] Schetz, J., Kush, E., and Joshi, P. (1980). Wave phenomena in liquid jet breakup in a supersonic crossflow. *AIAA journal*, 18(7):774–778.

[66] Schetz, J. A. and Padhye, A. (1977). Penetration and breakup of liquids in subsonic airstreams. *AIAA J*, 15(10):1385–1390.

[67] Sembian, S., Liverts, M., Tillmark, N., and Apazidis, N. (2016). Plane shock wave interaction with a cylindrical water column. *Physics of Fluids*, 28(5):056102.

[68] Shukla, R. K. (2014). Nonlinear preconditioning for efficient and accurate interface capturing in simulation of multicomponent compressible flows. *Journal of Computational Physics*, 276:508–540.

[69] Shukla, R. K., Pantano, C., and Freund, J. B. (2010). An interface capturing method for the simulation of multi-phase compressible flows. *Journal of Computational Physics*, 229(19):7411–7439.

[70] Shyue, K.-M. and Xiao, F. (2014). An eulerian interface sharpening algorithm for compressible two-phase flow: the algebraic thinc approach. *Journal of Computational Physics*, 268:326–354.

[71] Smirnov, A., Shi, S., and Celik, I. (2001). Random flow generation technique for large eddy simulations and particle-dynamics modeling. *Transactions of the ASME-I-Journal of Fluids Engineering*, 123(2):359–371.

[72] Tabor, G. and Baba-Ahmadi, M. (2010). Inlet conditions for large eddy simulation: A review. *Computers & Fluids*, 39(4):553–567.

[73] Toro, E. F. (2009). *Riemann solvers and numerical methods for fluid dynamics: a practical introduction*. Springer-Verlag.

[74] Toro, E. F., Spruce, M., and Speares, W. (1994). Restoration of the contact surface in the hll-riemann solver. *Shock waves*, 4(1):25–34.

[75] Urbin, G. and Knight, D. (2001). Large-eddy simulation of a supersonic boundary layer using an unstructured grid. *AIAA journal*, 39(7):1288–1295.

[76] Wu, P., Hsiang, L., and Faeth, G. (1995). Aerodynamic effects on primary and secondary spray breakup. *Liquid rocket engine combustion instability(A 96-11301 01-20), Washington, DC, American Institute of Aeronautics and Astronautics, Inc.(Progress in Astronautics and Aeronautics.)*, 169:247–279.

[77] Wu, P.-K., Kirkendall, K. A., Fuller, R. P., and Nejad, A. S. (1997). Breakup processes of liquid jets in subsonic crossflows. *Journal of Propulsion and Power*, 13(1):64–73.

[78] Xiao, F., Dianat, M., and McGuirk, J. J. (2013). Large eddy simulation of liquid-jet primary breakup in air crossflow. *AIAA journal*.

[79] Xiao, F., Ii, S., and Chen, C. (2011). Revisit to the thinc scheme: a simple algebraic vof algorithm. *Journal of Computational Physics*, 230(19):7086–7092.

[80] Xiao, F., Wang, Z., Sun, M., Liang, J., and Liu, N. (2016). Large eddy simulation of liquid jet primary breakup in supersonic air crossflow. *International Journal of Multiphase Flow*, 87:229–240.

[81] Xiong, Z., Nagarajan, S., and Lele, S. K. (2004). Simple method for generating inflow turbulence. *AIAA J*, 42(10):2164–2166.

[82] Xu, S. and Martin, M. P. (2004). Assessment of inflow boundary conditions for compressible turbulent boundary layers. *Physics of Fluids*, 16(7):2623–2639.

[83] Yates, C. (1972). Liquid injection into a supersonic stream. Technical report, AIR FORCE AERO PROPULSION LAB WRIGHT-PATTERSON AFB OH.